Article

Hydrogeochemistry of Fault-Related Hot Springs in the Qaidam Basin, China

Jie Tang [1,2], Xiaocheng Zhou [3,*], Yongxian Zhang [3,*], Jiao Tian [3], Miao He [3], Jingchao Li [3], Jinyuan Dong [3], Yucong Yan [3], Fengli Liu [3], Shupei Ouyang [3] and Kaiyi Liu [4]

[1] Hongshan National Observatory on Thick Sediments and Seismic Hazards, Xingtai 055350, China
[2] Hebei Earthquake Agency, Shijiazhuang 050021, China
[3] Institute of Earthquake Forecasting, China Earthquake Administration, Beijing 102628, China
[4] University of Sydney Business School, Sydney 2006, Australia
*   Correspondence: zhouxiaocheng188@163.com (X.Z.); yxzhseis@sina.com (Y.Z.)

Abstract: Hydrogeochemical characterization studies are regarded as an important method for determining the origin of hot springs. The major elements, trace elements, and stable isotopes of four groups of hot spring water samples and two groups of gas samples collected from the intersection of the Altyn Tagh fault zone and the East Kunlun fault belt were investigated in this study. The hot spring water temperature ranged between 6 °C and 14 °C. The water chemistry types of the hot springs were Na·Mg-Cl, Mg·Na-Cl·HCO$_3$, Na-Cl·SO$_4$, and Na-Cl·HCO$_3$. The δD values ranged from −50.00% to −68.60%, while the δ^{18}O values ranged from −6.90% to −8.60%. The hot spring water was recharged mainly by infiltrating precipitation, with a recharge elevation of 3390~3676 m. The heat storage temperature ranged from 66.7 to 164.9 °C. The circulation depth was estimated to range between 1043 and 2679 m. The strontium isotopic composition of the water samples in response to the main weathering sources comprised carbonate and sulfate. CO$_2$ was the main component in the hot spring gas in the study region, and its content was over 95%. The ^{3}He/^{4}He-R/Ra relationship diagram revealed that the mantle-sourced helium from the Yitunbulake spring was 3.06%. In comparison, that from the Aiken spring was 7.38%, which indicated an intrusion of mantle-source material mixed into the hot springs in the study region. The crustal marine limestone contributed significantly to the carbon inventory of the hot spring gas samples (>75%). The dissolution of the marl aquifer resulted in the release of CO$_2$. Carbon was primarily obtained through metamorphism and hydrothermal reactions in the basement lithologies. The Yitunbulake and Aiken hot springs are found near the intersection of the Arjin and East Kunlun fractures, where the water–rock response is relatively strong and the depth of circulation and thermal storage temperature are both high. This causes relatively high ambient pressure to be released from the deep fluid, resulting in microseismic activity in this region. The continuous observation of Aiken spring water chemistry allows for the monitoring of fracture activity in the region. The results of the study could serve as a foundation for further exploration of the relationship between geothermal water and deep faults, shallow geological formations, hydrogeological conditions, and geothermal resource development in the region.

Keywords: hot spring; isotopes; hydrogeochemistry; gas geochemistry; Altun Tagh fault; Kunlun fault belt

1. Introduction

Hot springs are the windows between the deep and shallow parts of the earth's crust, which are exposed mostly along the fracture zones and are also related to deep groundwater circulation systems. Therefore, the water chemistry and isotopic characteristics of hot springs reflect a variety of information regarding the geological structure, the stratigraphic lithology, and water–rock interaction during formation [1]. The distribution of a few hot springs is controlled by regional major fractures, particularly the active major fractures.

One reason for this is the permeability of the fractures. Another significant factor is that large regional fractures cut deeper. Meanwhile, the fracture zone rocks are broken, resulting in the formation of fissures that provide space and channels for groundwater storage and transportation [2]. Due to the different hydrogeological conditions of the fracture zone, geothermal fluids located at different parts of the fracture zone often exhibit different water circulation characteristics and water–rock interactions in regional deep and large fractures, resulting in different hydrochemical and thermal storage characteristics of the exposed hot springs [3]. Hot springs frequently circulate to depths of several kilometers, using the head of the water as a driving force, migrating upward along channels formed by angled, highly permeable fracture zones and becoming exposed to the surface [4,5]. Based on the components of He, Ne, Ar, N2, and CO_2 in hot springs, the distribution of the tectonic background, the degassing of Earth, the distribution of the crust–mantle heat flow, and other geological hot topics have been studied [6,7]. Several scholars have studied the relationship between the spatial and temporal variations in the helium and carbon isotopes of hot spring gases and fracture activities in non-volcanic fracture regions. It has been revealed that regions with strong fracture activities serve as good channels for deep material transport. The regions with high hot spring gas isotope ratios within active fracture zones usually exhibit significantly high-conductivity and low-velocity zones at their depths [8–10]. Therefore, helium isotope and carbon isotope analyses of hot spring gases in active fracture zones allow for the quantitative characterization of the mantle-origin mixture of helium and carbon dioxide in different ratios. Hot springs are naturally exposed underground hot water resources and serve as a kind of mineral resource with both natural and social significance. Therefore, hot springs are considered important material resources for the economic and social development of a particular region. Consequently, the hydrogeochemical characteristics of hot springs have been of interest to scholars in recent years. Several scholars have combined hydrogeochemical methods with gas and isotopic geochemical methods to study the source of underground hot water and the mixing of water from different sources [11–13].

The Altyn Tagh fault zone and the East Kunlun fault belt intersect at the southwest rim of the Qaidam Basin, a region rich in mineral resources and containing hot springs exposed along the fracture zones, including the highly active Aiken spring. Previous studies focused solely on the amount of water gushing from the hot springs, leaving out further investigation and analysis into the hot springs' genesis, chemical composition, and underlying formation mechanism. Therefore, the main study objects of this study were four typical hot springs distributed in this region of the fracture zone. The study looked at the ionic and isotopic properties of hot springs, as well as the geochemical properties of hot spring gases and the regional geological structure, the hot springs' recharge source, the recharge elevation, the water–rock interaction, the thermal storage temperature, and the circulation depth. The study results regarding the hydrogeochemical characteristics of the hot springs in the study region could provide a comprehensive understanding of the formation-related factors and the genesis types of these hot springs, while also serving as a scientific basis for the development and utilization of geothermal resources in the study region.

2. Geological Structural Background of the Study Region

The Qaidam Basin is the largest active inter-mountain basin on the Tibetan Plateau. It is a Meso-Cenozoic flexural basin that developed gradually under intense compression caused due to the long-term tectonic plate activities of the Qinghai–Tibet Plateau. The basin stretches 850 km from east to west and 150~300 km from north to south, with a total area of approximately 120,000 km^2 and an average elevation of approximately 3 km. In the middle of the Mesozoic Era, the uplift of the Kunlun Mountains caused the Qaidam region to gradually transition away from a marine environment. The frequent crustal movements led to the development of several faults and folds around the Qaidam region. The Qaidam Basin is one of the large-scale multi-energy terrestrial sedimentary basins in China, which has developed thick Cenozoic terrestrial sedimentary rocks. The formation and evolution

of the Qaidam Basin were jointly controlled by the Qilian Mountains tectonic zone, the Altyn Tagh fault zone, and the East Kunlun fault belt. The region has witnessed an uplift in the Qinghai–Tibet Plateau (Kunlong Mountain), left-wing movement of the Altyn, and an evolutionary history of sedimentary filling, which is why it is considered a research hotspot by domestic as well as foreign scholars [14–17]. The Qaidam Basin has been a large intracontinental depression with no foreland basin development since the Cenozoic period. Its sedimentary center is located on its central axis, with west-to-east migration [18]. The Cenozoic sedimentary strata are heavily covered in the central and southern parts of the basin, while they are exposed on the northern and western margins of the basin. The Cenozoic period witnessed exposure of the strata, with a total thickness of approximately 5271 m in the Dahonggou section located in the Qaidam Basin, which may be divided into the following six formations: the Lulehe formation, the Lower Ganchaigou formation, the Upper Ganchaigou formation, the Lower Youshashan formation, the Upper Youshashan formation, and the Shizigou formation. The groups are mostly in integrated contact with each other in the interior of the basin, with angular unconformity surface regions in the marginal areas of the basin [19–22]. In recent years, different methods have been employed to explore the sedimentary and tectonic characteristics of the Qaidam Basin from different perspectives, and considerable progress has been achieved [23–26].

The study region is located at the intersection of the Altyn Tagh fault zone and the East Kunlun fault belt, which belongs to the southwest rim of the Qaidam Basin (Figure 1b). The East Kunlun is located along the northern margin of the Qinghai–Xizang (Tibet) Plateau. It is a composite orogenic belt with multi-stage tectonic evolution [27,28]. The belt may be divided into the northern East Kunlun tectonic belt, the central East Kunlun ophiolatry melange belt, the southern East Kunlun tectonic belt, and the Buqingshan–A'nyemaqen ophiolitic belt (from north to south) [29–31]. With the occurrence of large-scale left-slip activity in the Altyn Tagh fault zone on the west side of the East Kunlun during the Middle Cenozoic period, the western section of the East Kunlun close to this fault zone was greatly modified. Since the Cenozoic period, a basin-ridge interval tectonic pattern has developed that differs significantly from the eastern section of the East Kunlun. The Qaidam Basin's northern boundary is formed of the Altyn Tagh Fault. It is a massive sinistral strike-slip fracture zone in the Asian continent that truncates various geological units, controlling both geometric characteristics and the tectonic framework in northern Tibet and playing an important role in regulating the tectonic deformation caused by the India/Eurasia collision [32,33]. The Altyn Tagh fault witnessed periods of strike-slip motion during the Cenozoic era, which were accompanied by an intense tectonic uplift. These strike-slip activities have influenced the Cenozoic tectonic evolution of the Qaidam Basin [34]. The late Quaternary slip rate was an average slip rate of 10~15 mm/year along the central portion of the Altyn Tagh fault, with a total displacement of approximately 350~400 km since the Phanerozoic period. The onset of the Cenozoic activity of this fault is generally considered to have occurred in the Late Eocene–Oligocene period [35–37].
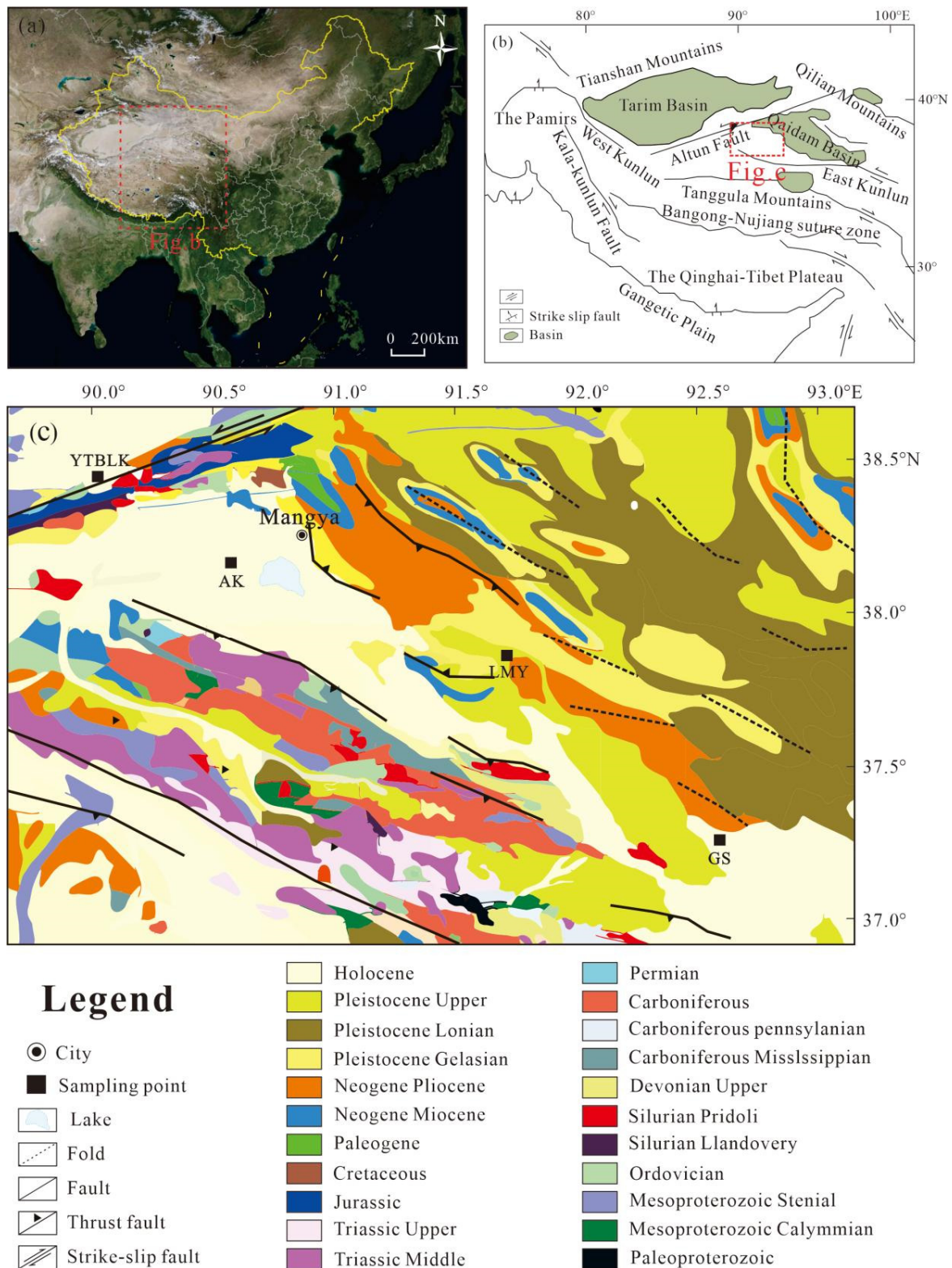
Figure 1. A plot depicting the sampling site distribution. (**a**) A geographical and spatial distribution map of China; base map: Google Earth satellite imaging map. (**b**) Tectonic unit division of the Qaidam Basin and its adjacent region. (**c**) The geological structure and the sampling points in the study region; base map: the 1:2,500,000 geological structure map of China.

3. Sampling Analysis: Methods and Results

In October 2020, water samples for chemical analysis were collected from four major hot springs (the Yitunbulake, Aiken, Laomangya, and Gansen (hereafter referred to as YTBLK, AK, LMY, and GS, respectively) along the intersection of the Altun Tagh fault and the East Kunlun fault belt (Figure 1c). A few field procedures were performed during sampling, including measuring water temperature, pH, and electrical conductivity (EC) using a portable measuring device WTW Multi 3400i (WTW, Munich, Germany) with precision of 0.1 °C, 0.01, and 1 s/cm for the three metrics, respectively. The device was calibrated with a standard solution before measurements were taken. In addition, basic information such as temperature, air pressure, and data on the surroundings was recorded. Samples were filtered in the field using a hand-held syringe with 0.45 mm membrane filters. The filtered samples were collected in fresh 100 mL polyethylene bottles and later subjected to analysis of their conventional ion components, trace elements, and SiO_2 content. The unfiltered samples were stored in HDPE plastic bottles and later subjected to isotope analyses. Prior to use, these bottles were rinsed with the sampling-point spring water to minimize the chances of contamination. The samples were then transported to the laboratory with proper care to prevent any possible effects of evaporation. Anions and cations were measured via high-performance ion chromatography using Dionex ICS-900 (Dionex, Sunnyvale, CA, USA) apparatus. The trace elements were determined using an X SERTES II (Thermo, Waltham, MA, USA) inductively coupled mass spectrometer. Hydrogen and oxygen isotopes were determined using a High-Temperature Conversion/Elemental Analyzer (TC/AE) coupled to an L2130-I Isotope Ratio Analyzer (Picarro, Santa Clara, CA, USA). The SiO_2 was determined using an inductively coupled Optima 5300 DV (Perkinelmer, Waltham, MA, USA) plasma emission spectrometer. The $^{87}Sr/^{86}Sr$ ratios were measured via thermal ionization mass-spectrometry using a Finnigan MAT-261 (ThermoFinnigan, Silicon Valley, CA, USA) spectrometer. The above experiments were conducted at the Key Laboratory of Earthquake Prediction, Institute of Earthquake Forecasting (China Earthquake Administration). All experiments were completed within 30 days of sampling.

The gas samples were collected in October 2020 from the YTBLK and AK springs with strong activity at the intersection of the Altun Tagh fault and the East Kunlun fault belt. Samples were collected in fresh 500 mL glass bottles using the drainage method. The N_2, H_2, CO_2, O_2, CH_4, and Ar components of the hot spring gas were measured using Agilent Macro 3000 (Agilent Technologies, Palo Alto, CA, USA) gas chromatography equipment. The estimated measurement errors were as follows: when the content was 1%~100%, the RSD was less than 0.5%; when the content was 0.01%~0.1%, the RSD was less than 1%; when the content was 0.001%~0.01%, the RSD was less than 2%; and when the content was 0.0001%~0.001%, the RSD was less than 5% [38]. The $^3He/^4He$ and $^4He/^{20}Ne$ ratios were analyzed using a Noblesse noble gas mass spectrometer produced by Nu Instruments, Wrexham, United Kingdom. Carbon dioxide isotopes were determined using a GC-IRMS analytical system gas chromatography (Agilent 6890, Agilent Technologies, Palo Alto, CA, USA) stable-isotope ratio mass spectrometer (Delta Plus XP, Thermo-Fisher Scientific, Waltham, MA, USA), coupled with an online sample preprocessor. The above experiments were conducted at the Oil and Gas Research Center of the North-West Institute of Eco-Environment and Resources (Chinese Academy of Sciences). All experiments were completed within 30 days of sampling.

The physical and chemical parameters of the hot spring samples are listed in Table 1. The temperatures of the water samples in the study region varied from 6.8 °C to 14 °C. The pH values of the spring water samples ranged between 6.81 and 7.75, which indicated a weak alkaline nature in general. The electrical conductivity values of the samples ranged from 1251 μs/cm to 10,090 μs/cm. The major cations were Na^+, Mg^{2+}, and Ca^{2+}, and the major anions were SO_4^{2-}, HCO_3^-, and Cl^-. The values of $\delta^{18}O$ ranged from -6.9% to -8.6%, while the δD values ranged from -50.0% to -68.6%. The silica content ranged from 7.23 mg/L to 52.22 mg/L. The contents of trace elements were relatively low.

Table 1. Sampling location and time, and physical and chemical composition of water samples.

Sampling Springs	YTBLK	AK	LMY	GS
Longitude (°)	90.0278 E	90.5786 E	91.7244 E	92.5959 E
Latitude (°)	38.3991 N	38.1166 N	37.8124 N	37.2100 N
Elevation (m)	2882	2848	2835	2814
Sampling date	2020.10	2020.10	2020.10	2020.10
Water temperature (°C)	9.7	14.0	6.8	9.5
PH	6.97	6.81	7.75	7.72
EC ($\mu s \cdot cm^{-1}$)	4910	10,090	2412	1251
Li^+ ($mg \cdot L^{-1}$)	2.50	0.96	0.05	0.00
Na^+ ($mg \cdot L^{-1}$)	6793	818.7	369.7	175.4
K^+ ($mg \cdot L^{-1}$)	268	15.01	12.94	7.52
Mg^{2+} ($mg \cdot L^{-1}$)	3459	661	39.70	19.50
Ca^{2+} ($mg \cdot L^{-1}$)	855.23	567.99	76.57	43.31
F^- ($mg \cdot L^{-1}$)	2.12	0.01	1.89	1.54
Cl^- ($mg \cdot L^{-1}$)	22,121	3087	524	238
Br^{2-} ($mg \cdot L^{-1}$)	0.00	8.65	0.00	0.65
SO_4^{2-} ($mg \cdot L^{-1}$)	4004	588	450	124
NO_3^{2-} ($mg \cdot L^{-1}$)	194	0.00	13.00	2.23
CO_3^{2-} ($mg \cdot L^{-1}$)	0.00	0.00	0.00	0.00
HCO_3^- ($mg \cdot L^{-1}$)	2055	2830	231	276
Chemical type	Na·Mg-Cl	Mg·Na-Cl·HCO$_3$	Na-Cl·SO$_4$	Na-Cl·HCO$_3$
Ag ($\mu g \cdot L^{-1}$)	0.045	0.017	0.023	0.02
Al ($\mu g \cdot L^{-1}$)	10.9	23.8	7.55	121
Ba ($\mu g \cdot L^{-1}$)	24.3	41.7	15.1	29.8
Be ($\mu g \cdot L^{-1}$)	0.16	0.765	0.035	0.01
Cd ($\mu g \cdot L^{-1}$)	0.848	0.069	0.063	0.041
Co ($\mu g \cdot L^{-1}$)	15	29.7	0.313	0.335
Cr ($\mu g \cdot L^{-1}$)	974	8.65	10.8	4.45
Cu ($\mu g \cdot L^{-1}$)	46.5	118	33.8	34.3
Fe ($\mu g \cdot L^{-1}$)	14,607	6849	117	390
Li ($\mu g \cdot L^{-1}$)	2005	870	58.2	26.5
Mn ($\mu g \cdot L^{-1}$)	2240	1617	2.23	9.47
Mo ($\mu g \cdot L^{-1}$)	0.067	0.207	7.77	5.8
Ni ($\mu g \cdot L^{-1}$)	74.6	62.9	7.41	4.41
Pb ($\mu g \cdot L^{-1}$)	0.633	0.949	0.494	0.783
Sb ($\mu g \cdot L^{-1}$)	0.154	0.087	0.046	0.121
Se ($\mu g \cdot L^{-1}$)	3.71	1.67	0.309	0.158
Sn ($\mu g \cdot L^{-1}$)	0.677	0.711	0.726	0.871
Sr ($\mu g \cdot L^{-1}$)	8995	11,620	1749	699
Th ($\mu g \cdot L^{-1}$)	17.4	0.029	0.003	0.036
Ti ($\mu g \cdot L^{-1}$)	410	6.8	1.77	8.42
U ($\mu g \cdot L^{-1}$)	65.3	92.9	10.4	10.7
V ($\mu g \cdot L^{-1}$)	183	54.2	15.2	9.37
Zn ($\mu g \cdot L^{-1}$)	28.3	28.2	13.2	16.2
B ($\mu g \cdot L^{-1}$)	12,407	878	605	285
SiO$_2$ ($mg \cdot L^{-1}$)	21.83	52.22	7.23	8.58
ΔD (‰)	−50.0	−68.6	−54.5	−56.8
δO (‰)	−6.9	−8.6	−7.9	−8.1

Table 2 lists the chemical parameters of the hot spring gas samples. CO_2 was the main component of the gas samples from both the YTBLK and AK hot springs, accounting for 95.43% and 99.58% of the total gas content, respectively. Furthermore, the samples contained low concentrations of He, H_2, CH_4, N_2, O_2, and Ar. Therefore, the hot springs in the study area were distinguished primarily by the relative enrichment of CO_2. The $^3He/^4He$ ratios of the samples from the two hot springs were 2.085×10^{-7} and 6.116×10^{-7}, respectively. The $^4He/^{20}Ne$ ratios of the samples were 768 and 164, respec-

tively. The $CO_2/^3He$ ratios of the samples were 29.56×10^9 and 44.98×10^9, respectively. The $\delta^{13}CCO_2$ (PDB) values of the samples were $-3.4‰$ and $-6.4‰$, respectively.

Table 2. Gas composition of the samples in the hot spring gases.

| Sampling Springs	He (ppm)	H$_2$ (ppm)	CO$_2$ (%)	CH$_4$ (%)	N$_2$ (%)	O$_2$ (%)	Ar (%)	^{3}He/^{4}He (10^{-7})	$_4$He/$_{20}$Ne	CO$_2$/$_3$He (10^9)	δ^{13}CCO$_2$ (‰, vs. PDB)
YTBLK	153	3.2	95.43	0.5185	5.02	0.49	0.026	2.085	768	29.56	−3.4
AK	36	5	99.58	0.0024	1.25	0.25	0.03	6.116	164	44.98	−6.4

4. Discussion

4.1. Hydrochemical Characteristics of the Hot Springs

4.1.1. Major Components in the Spring Water

The results of the study revealed that the average EC value of the samples was 4665.8 μS/cm. These values were particularly high for the AK spring samples. This high EC is actually primarily determined by the content of major anions and cations that are usually incorporated into the water via geochemical processes, such as ion exchange, evaporation, and silicate weathering. A second factor that plays a role in EC is the temperature, as specific ion conductivity increases with temperature. Water temperature is indeed higher in AK than in YTBLK, and this could explain part of the twofold increase in EC, in spite of the significantly higher ion concentrations in YTBLK. The dominating cations in the hot spring water at the sampling sites were the Na$^+$ ions. The normality concentration of Mg^{2+} ions in the YTBLK spring sample was relatively high. The normality concentrations of Ca^{2+}, Na$^+$, and Mg^{2+} ions in the AK spring samples were also relatively high. The cation compositions of the LMY and GS springs were relatively consistent, with the percentage of the Na$^+$ ion normality concentration reaching over 60% (Figure 2a). The main anion in the TYBLK spring water was Cl$^-$, which accounted for approximately 60% of the total anions, and its salinity was also relatively high. The main anions in the AK spring water were HCO$_3^-$ and Cl$^-$. The main anion in the LMY spring water was SO$_4^{2-}$, which accounted for approximately 50% of the total anions. The main anions in the GS spring water were HCO$_3^-$ and SO$_4^{2-}$ (Figure 2b). The main elements in the hot springs located at the Wenquan Ditch of Da Qaidam Area were Na, Cl, and SO$_4^{2-}$, and this composition is relatively similar to the chemical composition of the hot spring water samples from the study region, all of which were relatively rich in Ca and low in Mg; this is a typical characteristic of several deep hot waters, such as the typical oil field water in the western Qaidam Basin and the Tibetan geothermal water [39]. The same phenomenon was discovered in a study of hot springs in Canada's White Lake Basin and Mexico's eastern volcanic belt, where the cations in the hot spring water were primarily Na, followed by Ca, with very low concentrations of other cations. The anions were dominated by Cl, SO$_4$, and HCO$_3$ [40,41]. This phenomenon could be linked to the distribution of geological formations and the lithology surrounding them. Different water types may be defined according to the composition of the water. The Piper diagram depicted in Figure 2c was constructed using AquaChem Scientific Software (AquaChem 11.0) and presents the relative concentrations of different ions in individual water samples. It may be observed that the hydrochemical components in the study region were spatially complex along the fracture. The Schuka Lev classification method for groundwater chemistry based on EXCELS was employed [42], and all water samples were classified into the following four chemical types: Na·Mg-Cl, Mg·Na-Cl·HCO$_3$, Na-Cl·SO$_4$, and Na-Cl·HCO$_3$ (Table 1). Magnesium ions were dominant among the cations detected in the AK and YTBLK spring water samples. The common sources of magnesium ions in natural water include dolomite, olivine, hornblende, etc., and also calcium carbonate (CaCO$_3$). The Mg(Ca)-HCO$_3$- and Ca(Mg)-HCO$_3$- type waters are usually only located in the distribution areas of dolomite or dolomitic limestone. Therefore, it was inferred that the western part of the region is formed of magnesium-bearing carbonate rocks in the presence of CO$_2$. The concentrations of HCO$_3^-$, SO$_4^{2-}$, and Cl$^-$ in the water samples

increased gradually from the east to the west direction in the hot springs in the study region. HCO_3^- is formed primarily through the dissolution of carbonates in sedimentary rocks and the weathering dissolution of aluminosilicate minerals (sodium feldspar and calcium feldspar) in magmatic and metamorphic rocks. The presence of SO_4^{2-} indicates the presence of gypsum ($CaSO_4^-H_2O$) in sedimentary rocks or that the environment in which underground hot water appears and migrates is an oxidizing environment. A high Cl^- concentration indicates that water is discharged directly from a deep thermal reservoir with minimal mixing or conduction cooling and that water is supplied from the deep-water reservoir. When analyzed from a spatial perspective, the type of water chemistry in the study region was demonstrated to be relatively complex. The hot spring ion content was relatively higher spatially on the west side of the region compared to the east side. This could be attributed to the different surrounding rocks distributed along the fracture zone and the different activities of the surrounding fractures.
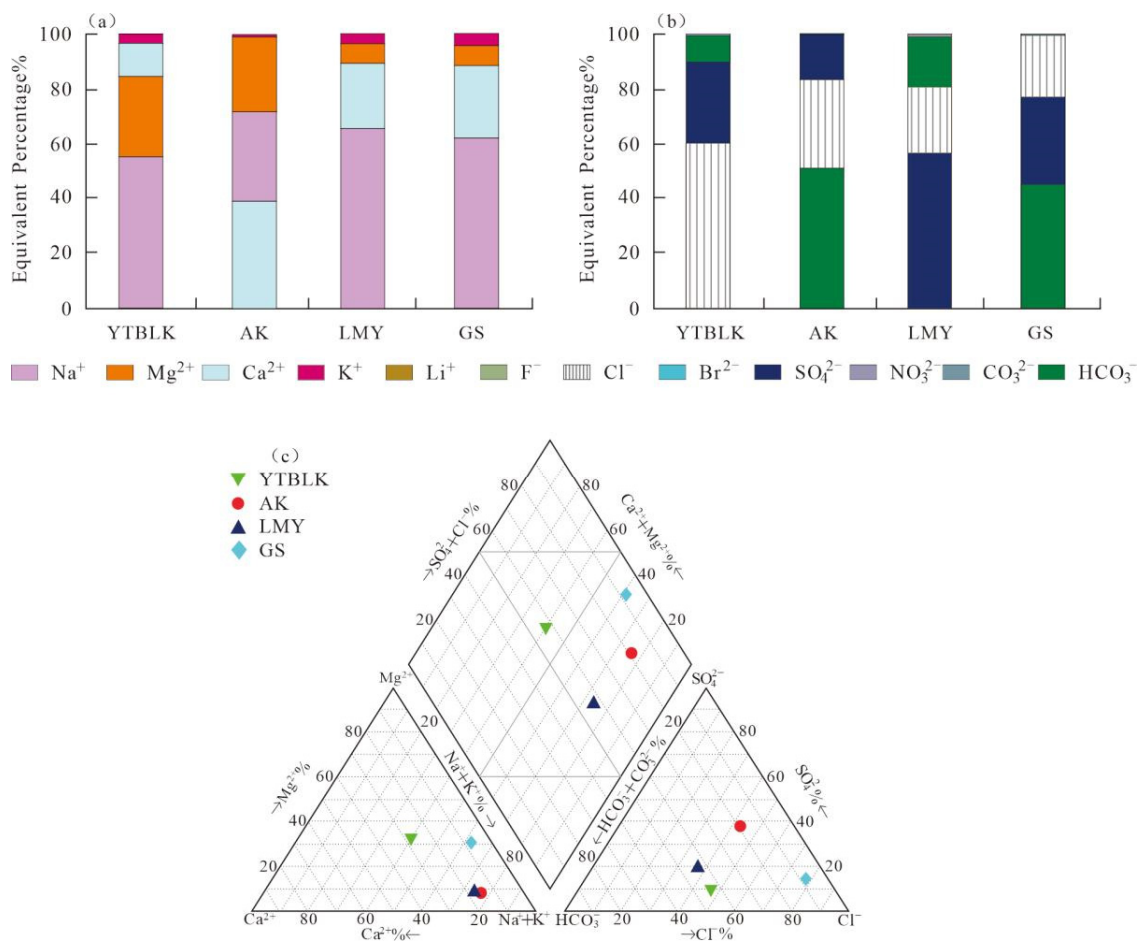

Figure 2. Ion concentration diagrams. (**a**) Percentage of major cations. (**b**) Percentage of major anions. (**c**) Piper diagram of sampling sites in study area.

To a certain extent, trace elements in hot springs reflect the degree of water–rock interaction in the groundwater. The presence of 24 trace elements, including Ag, Al, Ba, Be, Cd, Co, Cr, Cu, Fe, Li, Mn, Mo, Ni, Pb, Sb, Se, Sn, Sr, Th, Ti, U, V, Zn, and B, was observed at the four hot spring sampling sites. Table 1 shows the trace element concentrations. The magnitude of trace element enrichment coefficients can be used to determine the source of trace elements in hot spring water, which is calculated as follows:

$$EF_i = (C_i/C_R)w/(C_i/C_R)r \tag{1}$$

In Equation (1), C_i denotes the elemental content in the sample, C_R denotes the content of the selected reference element, W denotes the elemental concentration in the water sample, and r denotes the elemental concentration in the rock. The enrichment coefficients reflect the degree of enrichment of a certain element in the region; the larger the enrichment coefficients, the more concentrated the element. The smaller the enrichment coefficients, the more dispersed the element.

Considering the information on the location and lithology of the study region, along with the findings of recent research, the regional average value of trace elements in the Upper Ganjigou Formation at the northwestern margin of the Qaidam Basin was selected as the standard value. The contents of Ba, Co, Cr, Cu, Fe, Mn, Ni, Pb, Sr, Th, Ti, U, V, and Zn in the rocks were 387.62, 13.92, 111.65, 31.88, 32600.42, 643.31, 36.46, 25.40, 289.77, 10.50, 147.00, 2.77, 93.08, and 103.40 μg/g, respectively [43]. Ti was selected as the reference element owing to its greater stability. The trace element data were normalized to calculate the enrichment factors of trace elements (EFs) in the study region. The enrichment factor of Sr in the hot spring water in the study region was the strongest (Figure 3). Sr is the most abundant element in celestite, a mineral found in dolomite, marl, limestone, and other rocks. This was based on the available drilling and logging data for the region, as well as the application of sedimentological theory. Bao et al. [44] investigated the sedimentary phases of the Lower Ganchagou Formation and discovered that the region's lithology was dominated by marl. Therefore, in the present study, it was inferred that the hot spring water of the study region mainly originated from the marl aquifer.
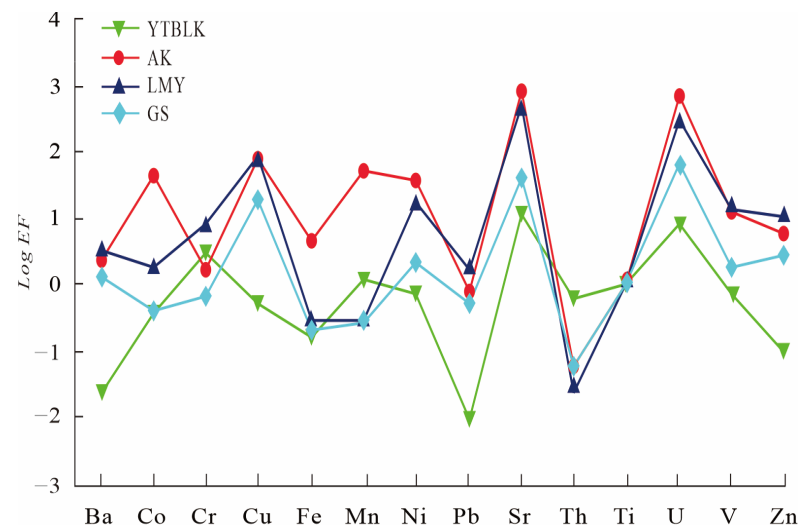
Figure 3. Enrichment coefficients of trace element in the hot springs.

4.1.2. Water–Rock Interaction

The relative contents of Na, K, and Mg in the thermal water in full equilibrium with a thermodynamically stable mineral system derived through the isochemical recrystallization of an average crustal rock remain, at a given temperature and salinity, uniquely fixed. These content values, along with the water compositions resulting from isochemical rock dissolution, are useful references for determining the degree of attainment of fluid–rock equilibrium [45]. According to the current study's findings, water samples from the study region were distributed below the partial balance line (Figure 4). The degree of water–rock interaction balance was relatively low, which could be attributed to ascent mixing with cold water [46]. The results for the AK and YTBLK spring water samples were closer to the partial equilibrium water line than those for the other spring water samples, indicating that they were closer to the water–rock equilibrium state. This also indicated that the cold-water mixing effect was relatively weak for these two springs. This could be attributed to the YTBLK and AK springs' spatial location, which is closer to the intersection of the Altun Tagh fault and the East Kunlun fault belt, where fracture activity is relatively high [47]. The

results for the other water samples were close to the immature water at the Mg terminal element, indicating that the water–rock interaction was low and a certain degree of shallow cold-water mixing occurred. In addition, the water samples in the study region reached equilibrium in the water–rock interaction at a lower temperature (Figure 4).
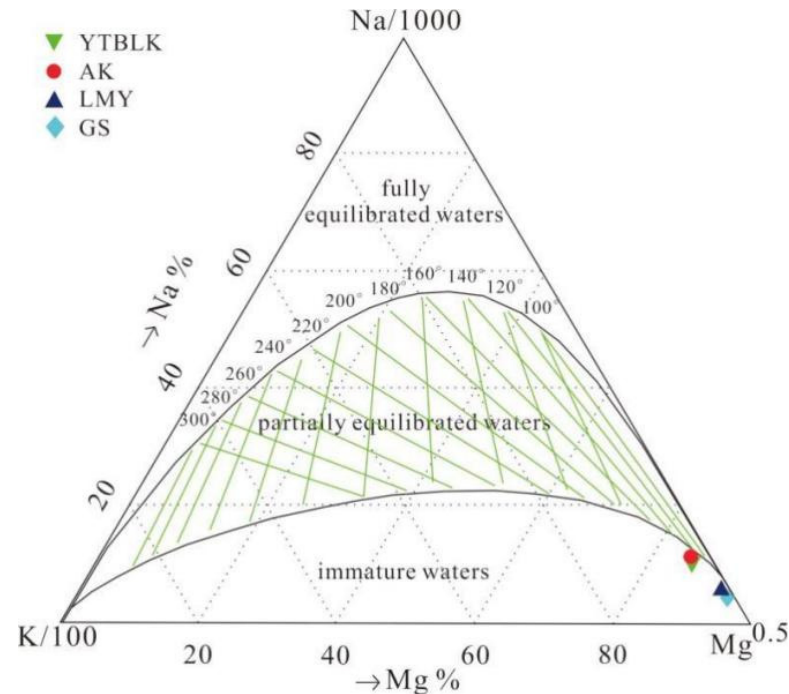

Figure 4. Distribution of aqueous samples shown on a Na/1000-K/100-Mg1/2 ternary diagram [45].

4.1.3. Origin of the Hot Spring Waters

Craig [48] proposed the Global Meteoric Water Line (GMWL) by providing the range of variation in the δD and δ^{18}O values in atmospheric precipitation and the relationship between them for various regions worldwide. The corresponding mathematical expression was as follows: δD = 8 × δ^{18}O + 10. This provided a basis for the isotopic exploration of groundwater recharge sources. However, due to the differences in the sources of water vapor and evaporation patterns in the circulation systems among different regions, the GMWL of the study region deviated from the regional atmospheric precipitation line (LMWL). In the present study, the northwest region was selected as the precipitation isotope reference site for the study region. The LMWL equation for the northwestern region was as follows: δD = 7.05 × δ^{18}O − 2.71 [49]. The figure depicting the δD-δ^{18}O relationships for the hot springs in the study region revealed that the isotope data for these hot springs were mainly distributed close to the regional atmospheric precipitation line (LMWL) of the northwestern region, indicating that the water of these hot springs originated primarily from meteoric water and interacts with geothermal fluids from confined aquifers that flow to the surface through fractures (Figure 5). A geothermal water study in the Sabalan volcano, NW Iran, discovered that the different degrees of δ^{18}O displacement of water samples resulted from an isotopic exchange between the geothermal fluid and the host rock in the geothermal reservoir [50]. AK springs exhibited positive displacement along the δ^{18}O axis from LMWL, indicating a relatively high degree of water–rock response in AK springs compared to other hot springs.

Since altitude varies widely in the Qinghai region, the maximum altitude difference at the sampling site was 633.26 m. Considering that the hydrogen and oxygen isotopes are affected by this altitude variation effect, the altitude effect of isotopes was utilized for the preliminary estimation of the water recharge altitude of the hot springs. The following equation was used:

$$H = (\delta G - \delta P)/k + h \qquad (2)$$
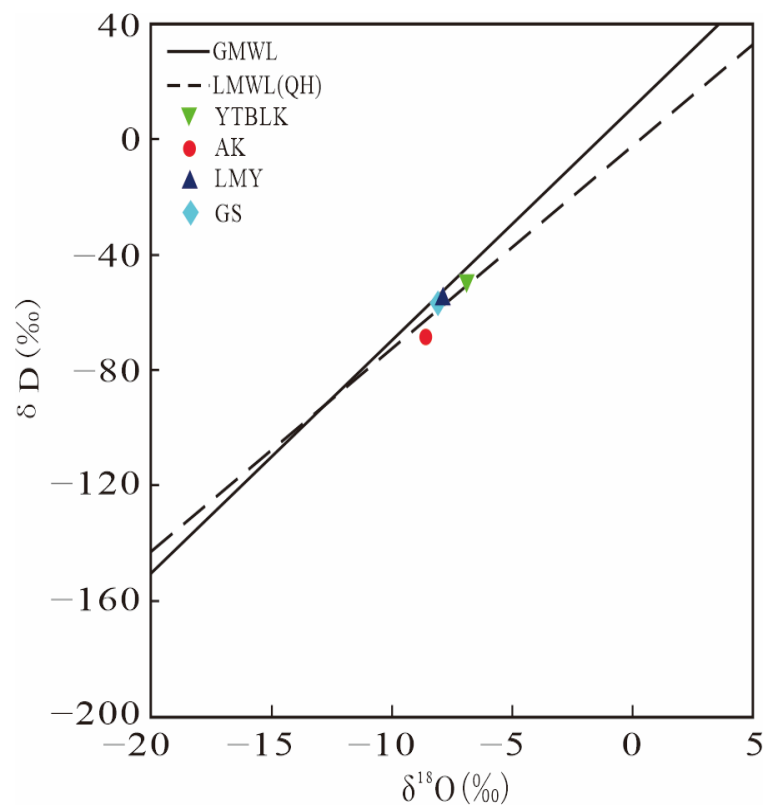
Figure 5. Stable oxygen and hydrogen isotopes of the water samples and their correlations with GMWL and LMWL.

In Equation (2), H denotes the elevation of the recharge region, h denotes the elevation of the sampling point, δG is the $\delta^{18}O$ (δD) value of carbonate springs, δP is the $\delta^{18}O$ (δD) value of atmospheric precipitation close to the sampling point, and k is the height gradient of the $\delta^{18}O$ (δD) value of atmospheric precipitation (‰/100 m). The global average $\delta^{18}O$ elevation gradient (k ($\delta^{18}O$) = −0.25‰/100 m) was used as the elevation gradient of the $\delta^{18}O$ (δD) values of atmospheric precipitation. The isotopically weighted average of atmospheric precipitation in Qinghai ($\delta^{18}O$ = −7.19) was used as the $\delta^{18}O$ value of atmospheric precipitation [51]. The recharge elevation of the hot springs in the study region was calculated using Equation (2). The results revealed that the recharge elevations for the YTBLK, AK, LMY, and GS springs were 3535 m, 3676 m, 3477 m, and 3390 m, respectively, among which the recharge elevation of the AK spring was relatively high (Table 3). Tyc et al. discovered a clear spatial correlation between hot springs and active fractures in the western Peruvian Cordillera, and that the tectonics provide pathways for hydrothermal solutions and gases that contribute to the heating of atmospheric water. Therefore, tectonic features play a significant role in the formation of hot spring water [52]. When combined with the topography and geomorphology of the study region, it was determined that the hot spring recharge in the study region was primarily caused by southern Alpine glacial meltwater and tectonic fractures.
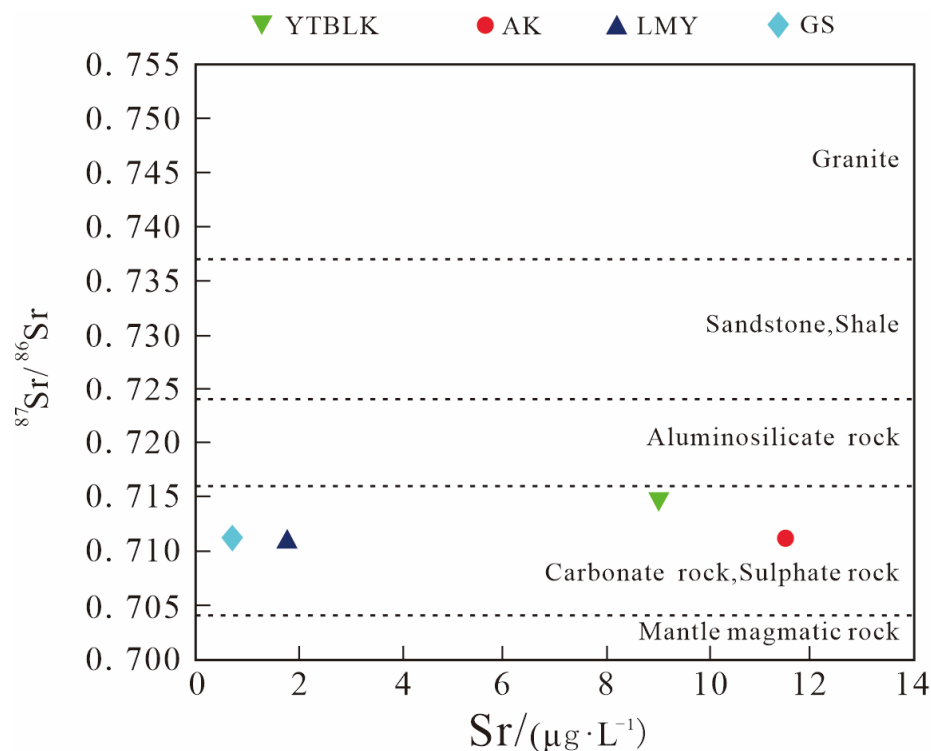
Table 3. Thermal storage temperature and circulation depth of hot springs in the study area.

Sampling Springs	The Quartz Silica Temperature Scale (°C)	The Chalcedony Temperature Scale (°C)	The α-Cristobalite Temperature Scale (°C)	Circulation Depth (m)
YTBLK	66.76	115.39	17.46	1854
AK	103.84	164.91	53.41	2679
LMY	29.11	66.74	−18.09	1043
GS	34.38	73.45	−13.17	1155

4.1.4. Strontium Isotope Analysis

The isotopic composition in hot spring water reflects the lithological characteristics of the strata through which the water flows. The Sr (strontium) concentration in the study region varied from 0.699 to 11.62 mg/L, with the highest content observed in the AK springs. The Sr^{2+} content in atmospheric precipitation is extremely low. Consequently, the water–rock interaction in the aquifer media during groundwater transport determines the Sr^{2+} content in the hot spring water [53]. The concentrations of Ca^{2+} and Sr^{2+} in the water samples from hot springs exhibited a good and positive correlation (Tables 1 and 2), mainly because calcium and strontium belong to the same group in the periodic table of elements and, therefore, have the same properties, such as isomorphism (the replacement of Ca with Sr). Therefore, in minerals with high calcium content, the content of strontium is also relatively high [54]. Ca substitution with Sr has also been found in hot water studies in northeastern Algeria [55].

Sulfate, silicate, and carbonate minerals are important sources of Sr in groundwater. The $^{87}Sr/^{86}Sr$ ratio of the hot spring is often similar to the $^{87}Sr/^{86}Sr$ ratio of the rock minerals it contacts [56,57]. It is generally accepted that the $^{87}Sr/^{86}Sr$ ratio for the mantle magma source is 0.70400, the $^{87}Sr/^{86}Sr$ ratio for the carbonate and sulfate weathering sources is approximately 0.70800, the $^{87}Sr/^{86}Sr$ ratio for the aluminosilicate weathering sources ranges between 0.71600 and 0.72000, the $^{87}Sr/^{86}Sr$ ratio for the sandstone and shale weathering sources is 0.72417, and the $^{87}Sr/^{86}Sr$ ratio for the granite weathering sources is 0.73719 [58]. The relationship between the $^{87}Sr/^{86}Sr$ ratio and the Sr content of the hot springs in the study region was analyzed. It was revealed that the main weathering sources of the water in these hot springs were carbonate and sulfate (Figure 6). The strontium isotope ratios of the hot springs varied less and remained almost at the same level, while the Sr content varied more. This could be due to the similarity of the surrounding rocks on the flow path and the different accumulation times [59].

Figure 6. Strontium isotopic composition of the water samples.

4.1.5. Thermal Storage Temperature and Circulation Depth

Thermal storage temperature is an important consideration when assessing geothermal resources. Thermal storage temperature scaling is commonly accomplished using two methods: cation temperature scaling and SiO_2 temperature scaling. In general, the cation temperature scaling method is used to calculate the thermal storage temperature of partial-equilibrium water [60]. The water samples in the present study region were in the 'immature water' state. Therefore, the SiO_2 temperature scale was adopted in the present study, and the calculations were performed using the following equations [61].

$$T = 1309/(5.19 - \lg S) - 273.15 \tag{3}$$

$$T = 1302/(4.69 - \lg S) - 273.15 \tag{4}$$

$$T = 1000/(4.78 - \lg S) - 273.15 \tag{5}$$

Equation (3) represents the quartz silica temperature scale, Equation (4) represents the chalcedony temperature scale, and Equation (5) represents the α-cristobalite temperature scale. T denotes the estimated thermal storage temperature (unit: °C) and S denotes the SiO_2 concentration (unit: $mg \cdot L^{-1}$). The following order was revealed by the calculation results: chalcedony temperature scale > quartz silica temperature scale > α-cristobalite temperature scale. The quartz silica temperature scale estimates ranged from 29.1 to 103.8 °C, the chalcedony temperature scale estimates ranged from 66.7 to 164.9 °C, and the α-cristobalite temperature scale estimates ranged from -18.1 to 53.4 °C. The result values from all three methods revealed that the AK springs had the highest thermal storage temperature (Table 3). The estimated temperature obtained using the α-cristobalite temperature scale had negative values, while the estimated temperature obtained using the quartz silica temperature scale estimates had relatively low values. Therefore, these two methods were ineffective for estimating thermal storage temperature in the study region. Furthermore, because the chalcedony temperature scale is frequently used to estimate thermal storage temperature, the estimated value obtained using the chalcedony temperature scale may reflect the thermal storage temperature in the study region. The circulation depth was estimated based on the local geothermal gradient and the estimated thermal storage temperature of the chalcedony temperature scale [62] using Equation (6) provided below:

$$H = (T - T_0)/g + h \tag{6}$$

In Equation (6), H denotes the circulation depth (km), T denotes the thermal storage temperature (°C), T_0 denotes the temperature of the constant temperature zone (the value used was 4.1 °C), h denotes the depth of the normal temperature zone (value used: 20 m), and g denotes the geothermal gradient (value used: 60 °C/km) [63]. The final circulation depth of the hot springs in the study region ranged from 1043 to 2679 m, while the AK spring water circulated at a deeper depth. The thermal storage temperatures and the circulation depths of the hot springs in the study region demonstrated spatially high west and low east characteristics. Due to geological factors in eastern Turkey (e.g., a relatively thick crust, low surface heat flux, and a lack of ideal cover units), the thermal storage temperature and depth of circulation of hot spring water were discovered to be different at different locations during a geothermal water study in eastern Turkey [64]. The underground hot water ditch in the geothermal region, which is also located in the uplift-fracture-type geothermal resources of Qinghai Province, has a thermal storage temperature in the range of 61–143 °C and a circulation depth in the range of 948–2314 m, calculated using chalcedony. When compared to the results obtained for the present study region, these thermal storage temperature and circulation depth values were relatively low [65]. This may be caused by the distribution of the surrounding geological formations and the greater responsiveness of the hot springs in the study region to information regarding the deeper parts of the region.

4.2. Chemical Characteristics of the Hot Spring Gas

4.2.1. Chemical Composition of the Hot Spring Gas

In volcanic regions and active fault zones, the gas escaping from hot springs often contains high concentrations of CO_2 [66,67]. CO_2 was also revealed as the main component of hot spring gas in the present study region, with a content of over 95%, and the AK hot spring gas had the highest CO_2 content of 99.58%. Then came N_2, with a content of 5.02% and 1.25%, respectively. Therefore, it was deduced that the hot springs in the study area were CO_2 enriched (Table 2). The snow water infiltrates along the crack, enters the deep regions, and dissolves the surrounding carbonate rock before being exposed to the surface for release, resulting in calcium carbonate deposition [68]. The N_2/Ar ratios obtained for the YTBLK and AK hot springs were 41.97 and 193.08, respectively, which differed significantly from the value reported for air (approximately 83). The N_2/O_2 ratios determined for the YTBLK and AK hot springs were 10.24 and 5.09, respectively; both values exceeded the dissolved ratio for the air or air-saturated water [69]. This indicated that the gas escaping from these hot springs did not originate entirely from the atmosphere, but rather, originated from other sources, as well. The contents of He in the water samples from the above two springs were 153 and 36 ppm, respectively. Both values were significantly higher than the content of He in the atmosphere (5 ppm), indicating that this helium did not have an atmospheric source.

4.2.2. Isotopic Characteristics of Helium and Neon

Helium gas in the hot springs has multiple origins and is the most sensitive geochemical tracer used to identify mantle-sourced gases. Since the $^3He/^4He$ values in the mantle source, crust source, and air have their respective characteristics, the corresponding sources may be further analyzed based on the $^3He/^4He$ values of the samples [70]. In order to estimate the proportions of mantle-derived helium (Hem), it was proposed that the Rm values should be corrected according to the atmospheric value of the $^3He/^4He$ ratio to exclude atmospheric contamination. This is expressed as R_c/R_a, where R_c denotes the $^3He/^4He$ value of the sample after the removal of atmospheric interference. The calibration method uses the following equation:

$$R_c = \frac{R \times \left(\frac{^4He}{^{20}Ne}\right)_V - R_a \times \left(\frac{^4He}{^{20}Ne}\right)_a}{\left(\frac{^4He}{^{20}Ne}\right)_V - \left(\frac{^4He}{^{20}Ne}\right)_a} \tag{7}$$

In Equation (7), R denotes the $^3He/^4He$ value of the sample, R_a denotes the atmospheric $^3He/^4He$, which is equal to 1.39×10^{-6}, $(^4He/^{20}Ne)_V$ denotes the $^4He/^{20}Ne$ value of the sample, and $(^4He/^{20}Ne)_a$ denotes the atmospheric $^4He/^{20}Ne$, which is equal to 0.318. The R_C values obtained for the gas samples from the YTBLK and AK hot springs were $0.1496\ R_a$ and $0.4389\ R_a$. Both values were less than 1 R_a, indicating the characteristics of upper crustal-sourced helium. The $^3He/^4He$ gas ratios in the Valles Caldera region, New Mexico indicate a deep magmatic source (R/R_a up to 6) [71]. The $^3He/^4He$ ratios of the hot springs in this study area are 2.085 and 6.116, and the values of the AK springs are close to those of Valles Caldera region. After excluding atmospheric helium interference, it was observed that $R_c/R_a > 0.1$, which suggested that mantle-sourced helium additions occur in the hot springs of the present study region [72,73]. Since the $^4He/^{20}Ne$-R/Ra relationships of the mantle, crust, and atmosphere are relatively fixed, a $^4He/^{20}Ne$-R/Ra diagram may be employed to visually and effectively discern the genesis and the source regions of the fluids and rare gas. $^3He/^4He = 1.39 \times 10^{-6}$, $^4He/^{20}Ne = 0.318$ in the atmosphere; $^3He/^4He = 12 \times 10^{-6}$, $^4He/^{20}Ne = 100,000$ in the mantle; $^3He/^4He = 0.\ 02 \times 10^{-6}$, $^4He/^{20}Ne = 100,000$ in the continental crust. The area between the two black lines represents the mixing of atmospheric, crustal, and mantle helium [74]. The percentage of mantle-sourced helium could then be calculated by casting the hot spring gas data into the $^4He/^{20}Ne$-R/Ra relationship diagram. The release of the mantle-sourced helium from the

YTBLK spring was 3.06%, and that from the AK spring was 7.38% (Figure 7). These results suggested an intrusion of mantle-sourced material in the study region. Large amounts of mantle-derived helium are evident in volcanic regions [75]. However, no active Cenozoic volcanoes have been located in the vicinity of the study region, which suggests that the mantle-derived helium in the study region did not have a volcanic release. The Altun Tagh fault and the East Kunlun fault belt serve as good channels for the upward transport of mantle-derived helium, with dilution of the mantle-source helium via upper crustal-source helium during the upward transport, and this phenomenon is also observed in the Xianshuihe fault [38].
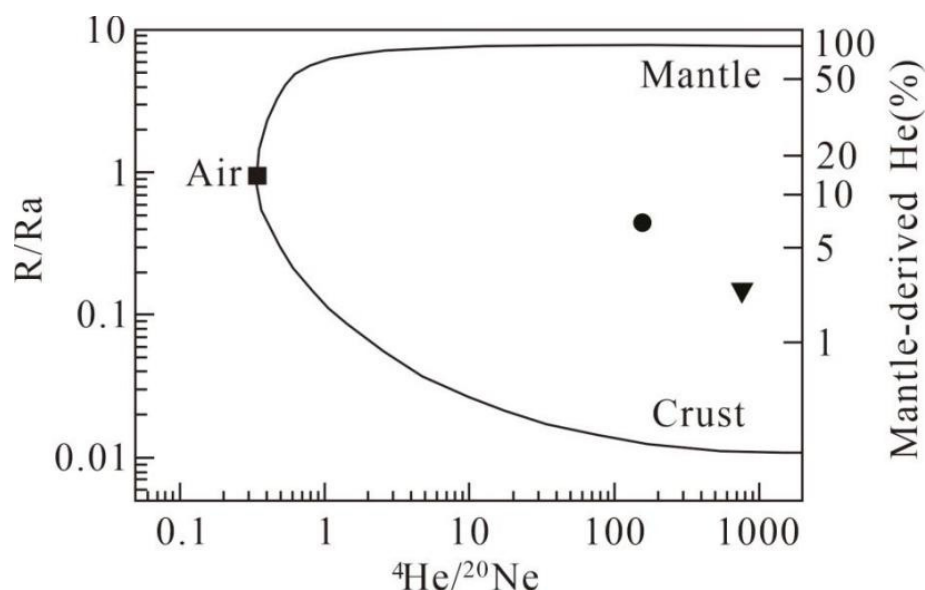

Figure 7. Plot of $^3He/^4He$ values vs. $^4He/^{20}Ne$ ratios of the hot spring gases.

A previous study on the rare gas isotopic signature of the northern margin of the Qaidam Basin in the eastern portion of the study region revealed $^3He/^4He$ values in the range of $(1.43–5.0) \times 10^{-8}$ and R/R_a values between 0.001 and 0.04, which are typical of upper crustal-sourced helium [76]. Faults are efficient conduits for gas transport, and the anomalous release of helium is often monitored before seismic activity, which, in addition to facilitating helium transport, serves as a physical factor influencing helium release in the formation [77,78]. Moreover, it is reported that the enrichment of ore bodies in the Qaidam Basin is controlled by the fracture system, which suggests that fractures, besides serving as good gas transport channels, are also a major influence on the generation of helium source rocks [79]. The study area is located at the intersection of the Altun Tagh fault and the East Kunlun fault belt, which is a large left-slip fault with deep basement penetration and a north-to-east trend, and this fault was active late in the Eocene and also underwent slip movement after that time [80]. The helium isotope content and ratio in the study region are largely comparable to those in the surrounding region. The source was from the mantle, which could be related to the fracture's distribution and activity. Future continuous observations of hot spring gas in the study region would, therefore, have research implications for monitoring seismic activity in the region.

4.2.3. Isotopic Characteristics of Stable Carbon

The carbon isotope characteristics in hot springs are governed by various geological-tectonic environments and different hydrogeological conditions, mainly depending on the CO_2 source and the storage environment of groundwater. The carbon isotope composition of carbonaceous compounds in the hot spring gas contains rich and important information [81,82]. The main types of CO_2 genesis in the hot springs are as follows: inorganic genesis and organic genesis. The CO_2 gases with different types of genesis

present different carbon isotope characteristics. The $\delta^{13}C_{CO2}$ values of the organic-genesis CO_2 are generally lower than −10‰, mainly −30‰ to −10‰, while the $\delta^{13}C_{CO2}$ values of inorganic-genesis CO_2 generally range from −8‰ to 3‰ [83]. Organic genesis is divided into two categories—biogenic and organic metamorphosis, which are usually transported from the outside. On the other hand, inorganic genesis occurs mainly through mantle magma and metamorphism. The $\delta^{13}C_{CO2}$ values of metamorphic genesis from carbonate rocks are close to those of carbonate rocks (approximately 0‰ ± 3‰), while the $\delta^{13}C_{CO2}$ values of volcanic–magmatic and mantle-derived genesis are in the range of −6‰ ± 2‰ [84,85]. Previous studies of the carbon isotopic composition of hot spring gases on the Tibetan Plateau have revealed that regional differences in carbon isotope compositions can be identified. The carbon in the samples from Yangbajain is lighter than in the samples from the northern sites. Carbon dioxide 13C values are comparable to mantle values, which range from −3 to −7‰ [86]. The $\delta^{13}C_{CO2}$ values of the hot spring gases in the current study region ranged from −3.4 to −6.4‰, which is more consistent with previous study results. Therefore, it was tentatively concluded that the hot spring gases in the study region had volcanic–magmatic and mantle-derived genesis. However, the carbon isotopes of the CO_2 gases from various sources in the hot spring gases overlapped. Consequently, the main source of CO_2 could not be directly derived from the carbon isotopes. CO_2 in the hot spring gases has greater isotopic fractionation in physicochemical processes than helium [81]. The relationship between $\delta^{13}C_{CO2}$ and the $CO_2/^3He$ ratio is used frequently to determine the source of CO_2 [87]. The proportions of mantle CO_2 in the gas samples of the study region were 5.06 and 3.32, which indicated intrusion of the mantle source material. It was apparent that crustal marine limestone was the major contributor to the carbon inventory of the hot spring gas samples (>75%), followed by sedimentary organic and mantle sources (Figure 8, Table 4). The CO_2 released from the dissolution of the marl aquifer and the metamorphism and hydrothermal reactions of the basement lithologies were the main sources of carbon in the hot springs in the study region. This was further closely related to the geology of the region because the sedimentary basement of the study region mainly comprised marl. This suggested that crustal additions exerted a strong influence on the samples.
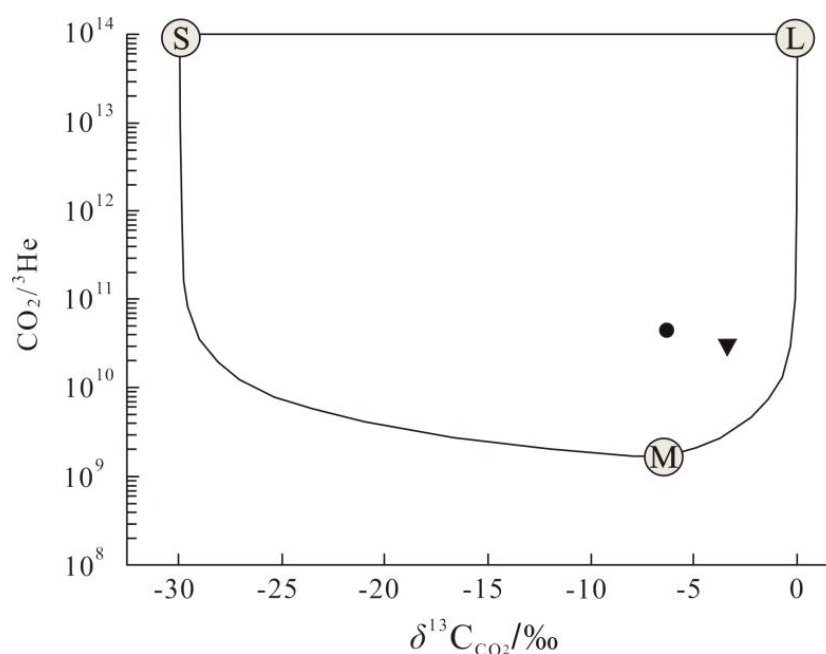
Figure 8. A plot of $CO_2/^3He$ values vs. $\delta^{13}C_{CO2}$ values obtained for the hot spring gases. The CO_2 sources of the hot spring gas were divided into three main source end elements—mantle carbon (M): $CO_2/^3He = 2 \times 10^9$, $\delta13C = -6.5‰$; limestone (L): $CO_2/^3He = 1 \times 10^{13}$, $\delta13C = 0‰$; and sedimentary organic carbon (S): $CO_2/^3He = 1 \times 10^{13}$, $\delta13C = -6.5‰$ [88,89].

Table 4. The CO_2 gas from mantle, limestone, and sedimentary sources in the hot spring gases of the study region.

Sampling Springs	Mantle Carbon (M)	Limestone (L)	Sedimentary Organic Carbon (S)
YTBLK	5.06	84.72	10.22
AK	3.32	76.09	20.59

4.3. Conceptual Model for Fluid Circulation

Hot springs are mostly exposed at the intersection of branch fractures and main fractures, which is the upper plate of extrusion fractures or deep-cut valleys formed due to fracture action. Geothermal water is recharged by infiltrating precipitation and heated by heat sources in the fracture system during the deep circulation process. Deep faults serve as a conduit not only for additional groundwater infiltration but also for the upward flow of deep geothermal fluids [90]. Understanding the origins and migration paths of springs in active fracture zones is critical for studying hydrogeochemical properties and geothermal resource extraction. Therefore, the present study's findings could be combined with existing geological data to construct a model.

The conceptual model of the hydrogeochemical cycle process of hot springs in the study region is illustrated in Figure 9. Hot springs are recharged mainly through atmospheric precipitation and glacial meltwater at 3390~3676 m. The recharge water seeps into the aquifer through hydraulic conductivity fractures between the mountains and the river terraces. The hot springs in the study region differed in spatial distribution, resulting in slight disparity in their recharge sources. The YTBLK and AK springs close to the intersection of the Altun Tagh fault and the East Kunlun fault had an evident recharge from fracture infiltration. In the study region, the Altun Tagh fracture zone and the East Kunlun fracture zone serve as good transport channels for the hot spring water, causing it to be transported downward along the fracture surface. Water–rock interactions with the enriched tuffs in the study regions occur during this transport process, producing small amounts of trace elements and larger macronutrients. Through geothermal heating, a portion of the hot spring water was transported downward to 1.04~2.68 km below the crust, and then, recharged upward to the hot springs around the fracture zone in the study region. The temperature of heat storage ranged from 66.7 to 164.9 °C. Water–rock interactions occur at various depths under certain temperature and pressure conditions. Spatially, the hot spring thermal storage temperature and circulation depth values were relatively large near the intersection of the Altun Tagh Fault and the East Kunlun fault belt zone, and the fracture intersection area was prone to high-stress-value anomaly zones. This indicated that the fracture controls fluid circulation and transport in this region. In addition, the microseismic activity in this region is relatively frequent, which is probably because the high degree of weakening of the water response here has weakened the fractures and rendered them further prone to earthquakes. Deeper fluid circulation and higher thermal storage temperatures in the hot springs lead to relatively high ambient pressure in the deeper fluids, causing microseismic activity in this region. In the process of a periodic rise, the circulating water may mix with colder surface water or shallow groundwater, eventually becoming hot springs that appear at the surface. In the present study, a water chemistry model was constructed for the hot springs in the study region. This model could serve as a geochemical basis for geothermal resource development. Strong tectonic movements and seismic activities may alter the subsurface stress–strain state and trigger the fragmentation of aquifers inside the fracture zone, leading to the mixing of deep fluids and shallow cold water; this then affects the degree of water–rock interactions of the underground hot water and changes the hydrochemical components and isotopic characteristics of the hot springs in the study region. This could provide evidence for short-term and upcoming earthquake prediction [91]. The hot spring water in the study region contains huge amounts of fugitive CO_2 gas. The fugitive CO_2 gas and the high-pressure fluid in the deep tectonic zone brought by the earthquake would exert a "lubricating" effect on the fault. In addition, according to the isotopic study of hot

spring gas in the study region, the hot spring gas samples had significant mantle source helium contribution. In regions with high helium gas isotope ratios in the hot springs of active fault zones, distinct zones of high conductivity and low velocity typically exist, suggesting that such fault zones are major conduits for helium degassing in the crust [92]. In fault zones, high-conductivity and high-velocity zones are thought to be fault rupture zones formed by impact sliding or shearing along the fault. Deep-source magma and/or metamorphic fluids fill these zones. Therefore, continuous monitoring of hot spring fluid geochemistry at the intersection of the Altun Tagh fault and the East Kunlun fault is critical for determining short-range fluid anomalies in this region and the surrounding regions to predict upcoming moderate-to-strong earthquakes.
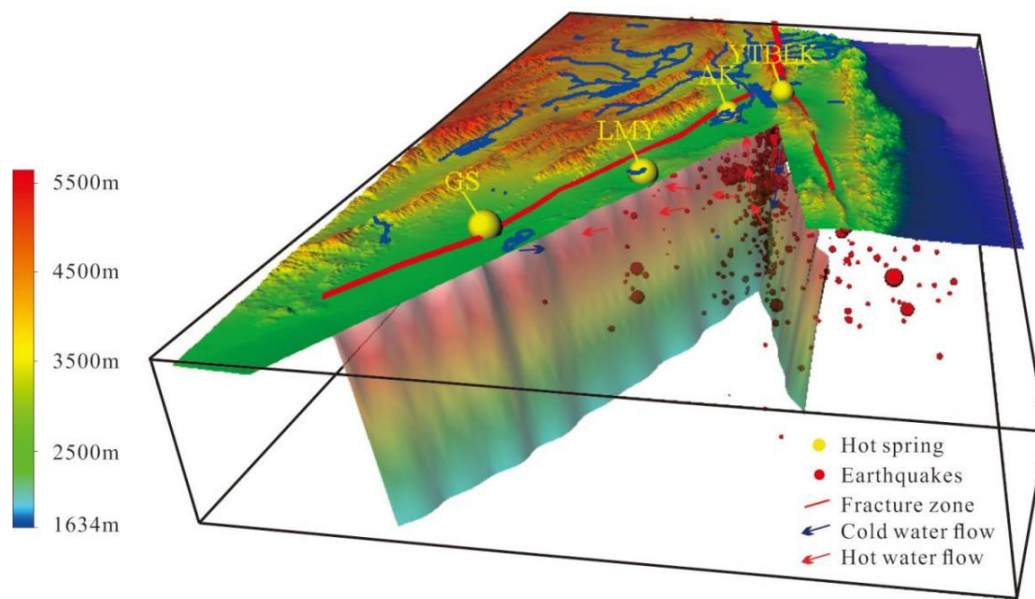
Figure 9. Conceptual model of the hot spring circulation in the study area.

4.4. Water Chemistry Anomalies and Regional Earthquake Response

Fluids are an important medium connecting the lithosphere, atmosphere, and biosphere. Fluids also play important roles in information transfer and material transfer in the geological evolution of Earth's interior [93,94]. Groundwater acts in the Earth's crust with a wide range and intensity, and its geochemical characteristics and genesis are closely associated with the geological environment and hydrogeological conditions of the region [95,96]. The chemical fraction of groundwater is governed mainly by the nature of the rocks it flows through, fracture tectonic activity, and deep-fluid supply, and factors such as seismic events might alter the chemical fraction of groundwater in a region [97–99]. According to studies, there is a close relationship between subsurface fluids and seismic activity. A series of fluid anomalies, such as water temperature, water level, and ion concentration, occur before and during moderate-to-strong earthquakes. During the earthquake precursor phase, hydrogeological and geochemical changes in wells or springs are observed, and subsurface fluid anomalies are clearly visible [100,101]. For example, K^+, Ca^{2+}, Mg^{2+}, and Cl^- concentrations increased significantly before the $M_S7.2$ earthquake that struck Van, Turkey, on 23 October 2011. The maximum values were reached 12 d before the earthquake, and the increase was nearly twofold [102]. Significant water chemistry anomalies related to Na^+, K^+, Ca^{2+}, Cl^-, and SO_4^{2-} were observed in the Beitianshan mud volcano and Shawan spring before and after the Xinyuan–Hejing $M_S6.6$ earthquake that occurred on 30 June 2012 [103]. Among the hot springs in the present study region, the hot spring that is most active in terms of external appearance is the AK spring, also referred to as the "Eye of the Earth" and the "Devil's Eye". The AK spring stretches to a diameter of over 10 m, and the

spring water is similar to boiling water, constantly tumbling upward. The sulfur minerals around the spring precipitated long ago (and have remained so to this day) and are colorful (Figure 10). The water chemical ion analysis results for the four hot springs in the study region revealed that the AK spring has a higher degree of trace element enrichment and a thermal storage temperature of 164.9 °C, which is typical of a marl thermal reservoir. The circulation depth reaches 2679 m, which is unusually high in comparison to other hot springs. Meanwhile, mantle-source material intrusion was discovered using gas isotope analysis. Therefore, when regional tectonic activity occurs, the AK spring generates more pore-fluid pressure during water circulation. The water–rock response is more intense, i.e., it responds better to regional tectonic activity and stress changes.

Figure 10. Schematic diagram of AK spring site visit. (**a**) AK spring top view. (**b**) AK spring 45° top view. (**c**) AK spring flat view.

An M_S5.5 earthquake occurred in the study region on 19 October 2022, close to the East Kunlun fault belt and spatially positioned 150 km southeast of the AK spring. Since May 2022, the project team has been conducting continuous measurements of the water chemistry ions at AK springs to continuously observe and collect data for the analysis of seismic efficiency. Water testing samples are collected at sampling points every 3 days and subjected to water chemistry measurements and mean-variance calculations. Any information pertaining to observed anomalies is documented. An anomaly is defined as a change in amplitude greater than ±2 times the mean variance. A positive high anomaly is defined as an increase in ion concentration that exceeds +2 times the mean-variance value. In contrast, a negative high anomaly is defined as a decrease that exceeds −2 times the mean-variance value. The negative ion concentration anomaly could be attributed to a relative increase in local atmospheric precipitation recharge and a relative decrease in fluids from deeper sources. The vast majority of seismic-fluid geochemical anomalies occur 3 months before and after an earthquake. These anomalies occur within a narrow range of distance, typically between 20 and 300 km from the epicenter [104]. The data processing results revealed that anomalies in Cl^-, Na^+, and SO_4^{2-} ion concentrations occurred in the AK spring at the end of June 2022 (Figure 11). Positive anomalies of varying degrees in the ion concentrations occurred in the study region, possibly related to the M_S5.5 (37.69 °N, 92.30 °E) earthquake that occurred on 19 October 2022. In the seismic gestation process, the deep fluid is transported upward along the fissure, and the water–rock interaction rate increases, causing the fluids containing Cl^-, Na^+, and SO_4^{2-} at depth to be mixed with shallow fluids, resulting in varying degrees of change in the subsurface fluid components. Therefore, changes in the chemical ion concentrations are an evident response to seismic activity and require enhanced monitoring. Moreover, to provide a reliable basis for earthquake prediction, further intensive sampling and analysis of this hot spring in different seasons over a long period are required to exclude the possibility of randomness.
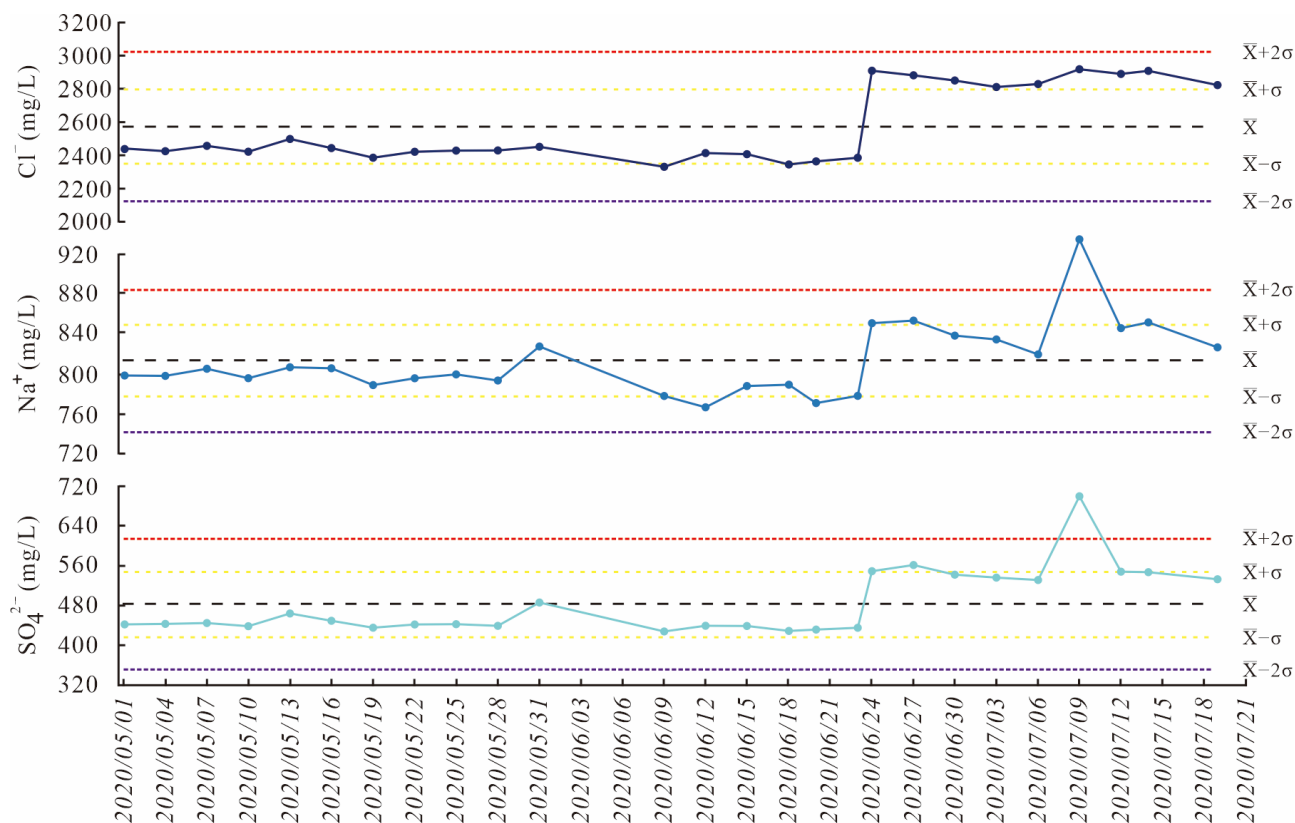
Figure 11. Time series diagram of AK spring ion detection results.

5. Conclusions

In the present manuscript, the hydrogeochemical and gas geochemical characteristics of hot springs in the study region were analyzed using four groups of water samples and two groups of gas samples, in addition to investigating the characteristics of the geological structure. The results of the study revealed the following:

(1) The water chemistry types of the hot springs in the study region were Na·Mg-Cl, Mg·Na-Cl·HCO$_3$, Na-Cl·SO$_4$, and Na-Cl·HCO$_3$. Water chemistry types were relatively complex, which could be attributed to the various surrounding rocks distributed along the fault zone. Sr emerged as the most powerful enrichment factor among the trace element enrichment factors. This discovery, combined with the findings of regional lithology analysis, indicated that the hot spring water in the study region was primarily derived from the marl aquifer. The analysis results for the water samples collected in the study region were distributed below the partial balance line, indicating that the degree of water–rock interaction balance was relatively low. This could be due to mixing with cold water during the ascent.

(2) The δD values ranged from −50.00% to −68.60%. The δ^{18}O values ranged from −6.90% to −8.60%. The hot spring water in the study region was recharged mainly through infiltrating precipitation, with a recharge elevation of 3390~3676 m. These results, combined with the topography and geomorphology of the study region, indicated that the hot spring recharge in the study region occurred mainly due to southern Alpine glacial meltwater and fracture recharge.

(3) The strontium isotope ratios of the hot springs varied less and remained nearly constant, whereas the Sr content varied more. This could be because of the similarity of the surrounding rocks along the flow path, as well as the different accumulation times.

(4) The thermal reservoir temperatures of the YTBLK, AK, LMY, and GS hot springs were 115.39, 164.91, 66.74, and 73.45 °C, respectively. The estimated range of circulation

depth for the hot springs at the intersection of the Altun Tagh fault and the East Kunlun fault was 1043~2679 m, while the AK spring circulated at a deeper depth. The thermal storage temperature and the circulation depth of the hot springs in the study region indicated a spatially high east and low west characteristic.

(5) CO_2 was the main component of hot spring gas in the study region, with a content of over 95%. The release of mantle-sourced helium from the YTBLK spring was 3.06%, and that from the AK spring was 7.38%. The results of the analysis indicated the presence of mantle-sourced material in the study region. The Altun Tagh fault and the East Kunlun fault belt are excellent channels for mantle-derived helium upward transport. The carbon inventory of the hot spring gas samples (>75%) was dominated by crustal marine limestone, followed by sedimentary organic and mantle sources. The CO_2 released from the dissolution of the marl aquifer, and the metamorphism and hydrothermal reactions of the basement lithologies, were the main sources of carbon in the hot springs of the study region.

Author Contributions: J.T. (Jie Tang), X.Z. and Y.Z. made equal contributions to this article by analyzing the data, and drafting and revising the manuscript. All authors contributed significantly to the interpretation of the results. All authors have read and agreed to the published version of the manuscript.

Data Availability Statement: Informed consent was obtained from all subjects involved in the study.

Conflicts of Interest: We declare that we have no known competing financial interests or personal relationships that could have appeared to influence the work reported in this paper.

References

1. Jayawardana, D.T.; Udagedara, D.T.; Silva, A.A.M.P.; Pitawala, H.M.T.G.A.; Jayathilaka, W.K.P.; Adikaram, A.M.N.M. Mixing geochemistry of cold water around non-volcanic thermal springs in high-grade metamorphic terrain, Sri Lanka. *Geochemistry* **2016**, *76*, 555–565. [CrossRef]
2. Zhou, X.; Jin, X.M.; Si, H.L.; Shen, H.; Zhang, H.M. *Monograph on Groundwater Science*, 2nd ed.; Geology Press Beijing: Beijing, China, 2017; pp. 1–245.
3. Lin, Y.W. A discussion on the relation of circulation depth of hot spring water to seismic activity on the northern segment of the Honghe fault zone. *Seismol. Geol.* **1993**, *15*, 193–200. [CrossRef]
4. Swanson, S.K.; Bahr, J.M.; Schwar, M.T.; Potter, K.W. Two–way cluster analysis of geochemical data to constrain spring source waters. *Chem. Geol.* **2001**, *179*, 73–91. [CrossRef]
5. Evans, M.J.; Derry, L.A. Hydrothermal flux of metamorphic carbon dioxide from the central Nepal Himalaya. In Proceedings of the AGU Fall Meeting, San Francisco, CA, USA, 8 December 2005. Abstracts.
6. Giggenbach, W.F.; Poreda, R.J. Isotopic composition of helium and CO_2 and CH_4 contents in gases produced along the New Zealand part of a convergent plate boundary. *Geochem. Cosmochem. Acta* **1993**, *57*, 3427–3455. [CrossRef]
7. Patterson, B.I.; Farley, K.A.; McInnes, A. Helium isotopic composition of geothermal gases phenocrysts and xenoliths from the Tabar-Lihir-Tanga-Feni Island arc, Papua New Guinea. *Geochim. Cosmochim. Acta* **1997**, *61*, 2485–2496. [CrossRef]
8. Italiano, F.; Martinelli, G.; Bonfanti, P.; Caracausi, A. Long-term (1997~2007) geochemical monitoring of gases from the Umbria-Marche region. *Tectonophysics* **2009**, *476*, 282–296. [CrossRef]
9. Umeda, K.; Ninomiya, A. Helium isotopes as a tool for detecting concealed active faults. *Geochem. Geophys. Geosyst.* **2013**, *10*, Q08010. [CrossRef]
10. Zmazek, B.; Italiano, F.Z.; Zivci, M.; Vaupotic, J.; Kobal, I.; Martinelli, G. Geochemical monitoring of thermal waters in Slovenia: Relationships to seismic activity. *Appl. Radiat. Isot.* **2002**, *57*, 919–930. [CrossRef]
11. Petrini, R.; Italiano, F.; Ponton, M.; Slejko, F.F.; Aviani, U.; Zini, L. Geochemistry and isotope geochemistry of the Monfalcone thermal waters (northern Italy): Inference on the deep geothermal reservoir. *Hydrogeol. J.* **2013**, *21*, 1275–1287. [CrossRef]
12. Busby, J. Geothermal energy in sedimentary basins in the UK. *Hydrogeol. J.* **2014**, *22*, 29–141. [CrossRef]

13. Afsin, M.; Allen, D.M.; Kirste, D.; Durukan, U.G.; Gurel, A.; Oruc, O. Mixing Processes in hydrothermal spring systems and implications for interpreting geochemical data: A case study in the Cappadocia region of Turkey. *Hydrogeol. J.* **2014**, *22*, 7–23. [CrossRef]

14. Harrison, T.M.; Copeland, P.; Kidd, W.S.F.; Yin, A. Raising Tibet. *Science* **1992**, *255*, 1663–1670. [CrossRef] [PubMed]

15. Yin, A.; Harrison, T.M. Geologic evolution of the HimalayanTibetan orogen. *Annu. Rev. Earth Planet. Sci.* **2000**, *28*, 211–280. [CrossRef]

16. Tapponnier, P.; Xu, Z.Q.; Roger, F.; Meyer, B.; Arnaud, N.; Wittlinger, C.; Sui, Y.J. Oblique stepwise rise and growth of the Tibet Plateau. *Science* **2001**, *294*, 1671–1677. [CrossRef] [PubMed]

17. Royden, L.H.; Burchfiel, B.C.; Hilst, R.D. The geological evolution of the Tibetan Plateau. *Science* **2008**, *321*, 1054–1058. [CrossRef]

18. Yin, A.; Dang, Y.Q.; Zhang, M.; Chen, X.H.; Rivette, M.W. Cenozoic tectonic evolution of the Qaidam Basin and its surrounding areas (Part 3): Structural geology, sedimentation and areaal tectonic reconstruction. *Eological Soc. Am. Bull.* **2008**, *120*, 847–876. [CrossRef]

19. Zhang, W.J. *The Sedimentary Studies of Cenozoic Paleoclimatic Events in the Northeastern Qaidam Basin*; Zhejiang University: Hangzhou, China, 2016.

20. Jiang, M.; Galvé, A.; Hirn, A.; Voogd, B.; Laigle, M.; Su, H.P.; Diaz, J.; Lépine, J.C.; Wang, Y.X. Crustal thickening and variations in architecture from the Qaidam Basin to the Qang Tang (North-Central Tibetan Plateau) from wide-angle reflection seismology. *Tectonophysics* **2006**, *412*, 121–140. [CrossRef]

21. Zhao, J.M.; Mooney, W.D.; Zhang, X.K.; Li, Z.C.; Jin, Z.J.; Okaya, N. Crustal structure across the Altyn Tagh Range at the northern margin of the Tibetan Plateau and tectonic implications. *Earth Planet. Sci. Lett.* **2006**, *241*, 804–814. [CrossRef]

22. Shi, D.N.; Shen, Y.; Zhao, W.J.; Li, A.B. Seismic evidence for a Moho offset and south-directed thrust at the easternmost QaidamKunlun boundary in the Northeast Tibetan Plateau. *Earth Planet. Sci. Lett.* **2009**, *288*, 329–334. [CrossRef]

23. Yin, A.; Dang, Y.Q.; Wang, L.C.; Jiang, W.M.; Zhou, S.P.; Chen, X.H.; Gehrels, G.E.; Rivette, M.W. Cenozoic tectonic evolution of Qaidam Basin and its surrounding areas (Part 1): The Southern Qilian Shan-Nan Shan thrust belt and northern Qaidam Basin. *Geological Soc. Am. Bull.* **2008**, *120*, 813–846. [CrossRef]

24. Fang, X.M.; Zhang, W.L.; Meng, Q.Q.; Gao, J.P.; Wang, X.M.; King, J.; Song, C.H.; Dai, S.; Miao, Y.F. High-resolution magnetostratigraphy of the Neogene Huaitoutala section in the eastern Qaidam Basin on the NE Tibetan Plateau, Qinghai Province, China and its implication on tectonic uplift of the NE Tibetan Plateau. *Earth Planet. Sci. Lett.* **2008**, *258*, 293–306. [CrossRef]

25. Lu, H.J.; Xiong, S.F. Magnetostratigraphy of the Dahonggou section, northern Qaidam Basin and its bearing on Cenozoic tectonic evolution of the Qilian Shan and Altyn Tagh Fault. *Earth Planet. Sci. Lett.* **2009**, *288*, 539–550. [CrossRef]

26. Zhang, W.L.; Fang, M.; Song, C.H.; Appel, E.; Yan, M.D.; Wang, Y.D. Late Neogene magnetostratigraphy in the western Qaidam Basin (NE Tibetan Plateau) and its constraints on active tectonic uplift and progressive evolution of growth strata. *Tectonophysics* **2013**, *599*, 107–116. [CrossRef]

27. Jiang, C.F.; Yang, J.S.; Feng, B.G.; Zhu, Z.Z.; Zhao, M.; Chai, Y.C.; Shi, X.D.; Wang, H.D.; Hu, J.Q. *Opening-Closing Tectonics of Kunlun Mountains*; Geological Publishing House: Beijing, China, 1992; pp. 1–224.

28. Yang, J.S.; Shi, R.D.; Wu, C.L.; Wang, X.B.; Robinson, P.T. The Dur'ngoi Ophiolite in East Kunlun, Northeast Tibetan Plateau: Evidence for a Paleo-Tethyan suture in Northwest China. *J. Earth Sci.* **2009**, *20*, 303–331. [CrossRef]

29. Meng, F.C.; Zhang, J.X.; Cui, M.H. Discovery of Early Paleozoic eclogite from the East Kunlun, Western China and its tectonic significance. *Gondwana Res.* **2013**, *23*, 825–836. [CrossRef]

30. Pei, X.Z.; Hu, N.; Liu, C.J.; Li, R.B.; Li, Z.C.; Chen, Y.X.; Pei, L.; Liu, Z.Q.; Chen, G.C.; Yang, J. Detrital Composition, Geochemical Characteristics and Provenance Analysis for the Maerzheng Formation Sandstone in Gerizhuotuo Area, Southern Margin of East Kunlun area. *Geol. Rev.* **2015**, *61*, 307–323.

31. Zhang, H.; Ma, C.Q.; Xiong, F.H.; Jiang, H.A.; Liu, B.; Guo, P. Two Contrasting Ophiolites in One Suture Zone: A Case Study form East Kunlun Orogenic Belt, North Tibetan Plateau. *Acta Geol. Sin.* **2016**, *89*, 111–112. [CrossRef]

32. Avouac, J.P.; Tapponnier, P. Kinematic model of active deformation in central Asia. *Geophys. Res. Lett.* **1993**, *20*, 895–898. [CrossRef]

33. Yin, A.; Rumelhart, P.E.; Butler, R.; Cowgill, E.; Harrison, T.M.; Foster, D.A.; Ingersoll, R.V.; Zhang, Q.; Zhou, X.Q.; Wang, X.F.; et al. Tectonic history of the Altyn Tagh fault system in northern Tibet inferred from Cenozoic sedimentation. *Geol. Soc. Am. Bull.* **2002**, *114*, 1257–1295. [CrossRef]

34. Pan, J.W.; Li, H.B.; Sun, Z.M.; Liu, D.L.; Wu, C.; Yu, C.Q. Tectonic responses in the Qaidam Basin induced by Cenozoic activities of the Altyn Tagh fault. *Acta Petrol. Sin.* **2015**, *31*, 3701–3712.

35. Yue, Y.J.; Ritts, B.D.; Graham, S.A. Initiation and long-term slip history of the Altyn Tagh Fault. International. *Geol. Rev.* **2002**, *43*, 1087–1093. [CrossRef]

36. Cowgill, E.; Gold, R.D.; Chen, X.H.; Wang, X.F.; Arrowsmith, J.R.; Southon, J. Low Quaternary slip rate reconciles geodetic and geologic rates along the Altyn Tagh fault, northwestern Tibet. *Geology* **2009**, *37*, 647–650. [CrossRef]

37. Mériaux, A.S.; Woerd, J.; Tapponnier, P.; Ryerson, F.J.; Finkel, R.C.; Lasserre, C.; Xu, X.W. The Pingding segment of the Altyn Tagh Fault (91° E): Holocene slip-rate determination from cosmogenic radionuclide dating of offset fluvial terraces. *J. Geophys. Res. Solid Earth* **2012**, *117*, B09406. [CrossRef]

38. Zhou, X.C.; Wang, W.C.; Chen, Z.; Yi, L.; Liu, L.; Xie, C.; Cui, Y.J.; Du, J.G.; Cheng, J.W.; Yang, L.M. Hot spring gas geochemistry in western Sichuan Province, China after the Wenchuan Ms 8.0 earthquake. *Terr. Atmos. Ocean. Sci.* **2015**, *26*, 361–373. [CrossRef]

39. Li, J.S. Geochemical Genesis of the Springs in Wenquan Ditch of Da Qaidam Area. *J. Salt Lake Res.* **2017**, *25*, 55–59.

40. Michel, F.A.; Allen, D.M.; Grant, M.B. Hydrogeochemistry and geothermal characteristics of the White Lake basin, South-central British Columbia, Canada. *Geothermics* **2002**, *31*, 169–194. [CrossRef]

41. Martínez-Florentino, T.A.K.; Esteller-Alberich, M.V.; Expósito, J.L.; Domínguez-Mariani, E.; Morales-Arredondo, J.I. Hydrogeochemistry and geothermometry of thermal springs in the eastern Trans-Mexican Volcanic Belt. *Geothermics* **2021**, *96*, 102176. [CrossRef]

42. Kou, W.J. Groundwater chemical Schuka Lev classification method based on EXCEL. *Geotechnical Investig. Surv.* **2013**, *5*, 48–50.

43. Ma, W.L.; Jiang, X.Q.; Li, X.; Zheng, L.; Yang, P.; Ma, J.L. Geochemical Characteristics and Paleoenvironment Paleoclimate Significance of Mudstone in the Shang-Gan-Chai-Gou Formation at the Northwestern Margin of Qaidam Basin.Bulletin of Mineralogy. *Petrol. Geochem.* **2021**, *40*, 1166–1180. [CrossRef]

44. Bao, J.C.; Guan, P.; Lei, T.; Fan, X.W. Determination of rational production-injection spacing by the degree of water flooding reserves in Gasikule oil field E reservoir. *Nat. Gas Geosci.* **2012**, *23*, 884–890. [CrossRef]

45. Giggenbach, W.F. Geothermal solute equilibria.Derivation of Na-K-Ma-Ca geoindicators. *Geochim. Cosmochim. Acta* **1988**, *52*, 2749–2765. [CrossRef]

46. Yao, Y.Z. *Analysis of Geological Characteristics and Genetic Model of Midu Hot Spring*; Kunming University of Science and Technology: Kunming, China, 2010. (In Chinese)

47. Wen, X.Z. Time dependent segmented seismic risk assessment of active faults and its problems. *Chin. Sci. Bull.* **1998**, *43*, 1457–1466. [CrossRef]

48. Craig, H. Isotopic variations in meteoric waters. *Science* **1961**, *133*, 1702–1703. [CrossRef]

49. Liu, J.R.; Song, X.F.; Yuan, G.F.; Sun, X.M.; Liu, X.; Chen, F.; Wang, Z.M.; Wang, R.Q. Characteristics of $\delta^{18}O$ in Precipitation over Northwest China and Its Water Vapor Sources. *Acta Geogr. Sin.* **2008**, *63*, 12–22.

50. Rezaei, A.; Rezaeian, M.; Porkhial, S. The hydrogeochemistry and geothermometry of the thermal waters in the Mouil Graben, Sabalan volcano, NW Iran. *Geothermics* **2019**, *78*, 9–27. [CrossRef]

51. Zhang, X.P.; Zhong, Z.Y.; Yao, T.D.; Han, J.K.; Xie, Z.C. Temporal and spatial variation of stable isotopic composition in precipitation over the Qinghai Xizang Plateau and its adjacent areas. *Sci. Sin.* **2001**, *31*, 353–361. [CrossRef]

52. Tyc, A.; Gaidzik, K.; Ciesielczuk, J.; Masías, P.; Paulo, A.; Postawa, A.; Zaba, J. Thermal springs and active fault network of the central Colca River basin, Western Cordillera, Peru. *J. Volcanol. Geotherm. Res.* **2022**, *424*, 107513. [CrossRef]

53. Tian, X.Z.; Shan, Q.; Song, L.Z. Analysis on chemical characteristics and evolution trend of groundwater in Tangshan Coastal Area. *South North Water Transf. Water Sci. Technol.* **2011**, *9*, 139–144. [CrossRef]

54. Tan, M.R.; Zhou, X.; Zhang, Y.Q.; Liu, H.S.; Yu, M.X.; Hai, K. Hydrochemical and isotopic characteristics and formation of the Mengajie hot spring in Menghai county of Yunnan. *Hydrogeol. Eng. Geol.* **2019**, *46*, 70–80. [CrossRef]

55. Chenaker, H.; Houha, B.; Vincent, V. Hydrogeochemistry and geothermometry of thermal water from north-eastern Algeria. *Geothermics* **2018**, *75*, 137–145. [CrossRef]

56. Philippe, N. Water–granite interaction: Clues from strontium, neodymium and rare earth elements in soil and waters. *Appl. Geochem.* **2006**, *21*, 1432–1454. [CrossRef]

57. Min, M.Z.; Peng, X.J.; Zhou, X.L.; Qiao, H.M.; Wang, J.P.; Zhang, L. Hydrochemistry and isotope compositions of groundwater from the Shihongtan sandstone-hosted uranium deposit, Xinjiang, NW China. *J. Geochem. Explor.* **2007**, *93*, 91–108. [CrossRef]

58. Edmond, J.M. Himalayan tectonics, weathering processes, and the strontium isotope record in marine limestones. *Science* **1992**, *258*, 1594–1597. [CrossRef] [PubMed]

59. Fisher, R.S.; Stueber, A.M. Strontium isotopes in selected streams within the Susquehanna River basin. *Water Resour. Res.* **1976**, *12*, 1061–1068. [CrossRef]

60. Fournier, R.O.; Rowe, J.J. he deposition of silica in hot springs. *Bull. Volcanol.* **1966**, *29*, 585–587. [CrossRef]

61. Fournier, R.O. Chemical geothermometers and mixing models for geothermal systems. *Geothermics* **1977**, *5*, 41–50. [CrossRef]

62. Sorey, M.L.; Colvard, E.M. Hydrologic investigations in the Mammoth Corridor, Yellowstone National Park and vicinity, U.S.A. *Geothermics* **1997**, *26*, 221–249. [CrossRef]

63. Fang, B.; Zhou, X.; Liang, S.H. Characteristics and utilization of the Zhacang hot springs in guide county Qinghai. *Geoscience* **1977**, *26*, 221–249. [CrossRef]

64. Aydin, H.; Karakuş, H.; Mutlu, H. Hydrogeochemistry of geothermal waters in eastern Turkey: Geochemical and isotopic constraints on water-rock interaction. *J. Volcanol. Geotherm. Res.* **2019**, *390*, 106708. [CrossRef]

65. Dai, M. *The Hydrogeochemical Characteristics and Evolution of Geothermal Water in Guide Area*; China University of Geosciences: Qinghai, China, 2020.

66. D'Alessandro, W.; De Gregorio, S.; Dongarrà, G.; Gurrieri, S.; Parello, G.F.; Parisi, B. Chemical and isotopic characterization of the gases of Mount Etna (Italy). *J. Volcanol. Geotherm. Res.* **1997**, *78*, 65–76. [CrossRef]

67. Du, J.G.; Liu, C.Q.; Fu, B.H.; Ninomiya, Y.; Zhang, Y.L.; Wang, C.Y.; Wang, H.L.; Sun, Z.G. Variations of geothermometry and chemical—isotopic compositions of hot spring fluids in the Rehai geothermal field, southwestern China. *J. Volcanol. Geotherm. Res.* **2005**, *142*, 243–261. [CrossRef]

68. Shen, L.C. *Study on Deep Degassing (Geology) and Carbon Cycle in Southwest China*; Southwest University: Chongqin, China, 2007. (In Chinese)

69. Weiss, R.F. The solubility of nitrogen, oxygen and argon in water and seawater. *Deep Sea Res. Oceanogr. Abstr.* **1970**, *17*, 721–735. [CrossRef]

70. Tao, M.X.; Xu, Y.C.; Shi, B.G.; Jiang, Z.X.; Shen, P.; Li, X.B.; Sun, M.L. Mantle degassing and deep geological structure characteristics of different types of fault zones in China. *Sci. Sin.* **2005**, *35*, 441–451. [CrossRef]

71. Goff, F.; Janik, C.J. Gas geochemistry of the Valles caldera region, New Mexico and comparisons with gases at Yellowstone, Long Valley and other geothermal systems. *J. Volcanol. Geotherm. Res.* **2002**, *116*, 299–323. [CrossRef]

72. Ballentine, C.J.; Marty, B.; Lollar, B.S.; Gassidy, M. Neon isotopes constrain convection and volatile origin in the Earth'smantle. *Nature* **2005**, *433*, 33–38. [CrossRef]

73. Duchkov, A.D.; Rychkova, K.M.; Lebedev, V.I.; Kamenskii, I.L.; Sokolova, L.S. Estimation of heat flow in Tuva from data on helium isotopes in thermal mineral springs. *Russ. Geol. Geophys.* **2010**, *51*, 209–219. [CrossRef]

74. Ozima, M.; Podosek, F.A. *Noble Gas Geochemistry*; Cambridge University Press: Cambridge, UK, 1983.

75. Xu, Z.Q.; Yang, J.S.; Li, W.C.; Li, H.Q.; Cai, Z.H.; Yan, Z.; Ma, C.Q. Paleo-Tethys system and accretionary orogen in the Tibet Plateau. *Acta Petrol. Sin.* **2013**, *29*, 1847–1860.

76. Han, W.; Liu, W.J.; Li, Y.H.; Zhou, J.L.; Zhang, W.; Zhang, Y.P.; Chen, X.H.; Huang, B. Characteristics of rare gas isotopes and main controlling factors of radon enrichment in the northern margin of Qaidam Basin. *Nat. Gas Geosci.* **2020**, *31*, 385–392. [CrossRef]

77. Holub, R.F.; Brady, B.T. The effect of stress on radon emanation from rock. *J. Geophysical Res. Solid Earth* **1981**, *86*, 1776–1784. [CrossRef]

78. Honda, M.; Kurita, K.; Hamano, Y.; Ozima, M. Experimental studies of He and Ar degassing during rock fracturing. *Earth Planet. Sci. Lett.* **1982**, *59*, 429–436. [CrossRef]

79. Chen, Q.; Liu, L.; Feng, W. Analysis of Uranium types and prospecting prospects in the northern margin of Qaid am Basin. *Geol. Rev.* **2015**, *61*, 464–465.

80. Xie, H.; Liu, C.C.; Zhang, H.P.; Zhan, Y.; Zhao, X.D. Cenozoic evolution of the Altyn Tagh fault:Evidence from sedimentary records of basins along the fault. *Acta Petrol. Sin.* **2022**, *38*, 1107–1125. [CrossRef]

81. Hilton, D.R. The helium and carbon isotope systematics of a continental geothermal system: Results from monitoring studies at Long Valley Caldera (California, U.S.A.). *Chem. Geol.* **1996**, *127*, 269–295. [CrossRef]

82. Kulongoski, J.T.; Hilton, D.R.; Barry, P.H.; Esser, B.K.; Hillegonds, D.; Belitz, K. Volatile fluxes through the Big Bend section of the San Andreas Fault, California: Helium and carbon-dioxide systematics. *Chem. Geol.* **2013**, *339*, 92–102. [CrossRef]

83. Dai, J.X. Identification of various genetic natural gases. *China Offshore Oil Gas Geol.* **1992**, *1*, 11–19.

84. Javoy, M.; Pineau, F.; Delorme, H. Carbon and nitrogen isotopes in the mantle. *Chem. Geol.* **1986**, *57*, 41–62. [CrossRef]

85. Sano, Y.; Wakita, H. Geographical distribution of 3He/4He ratios in Japan: Implications for arc tectonics and incipient magmatism. *J. Geophys. Res.* **1985**, *90*, 8729–8741. [CrossRef]

86. Yokoyama, T.; Nakai, S.; Wakita, H. Helium and carbon isotopic compositions of hot spring gases in the Tibetan Plateau. *J. Volcanol. Geotherm. Res.* **1999**, *88*, 99–107. [CrossRef]

87. Sano, Y.; Marty, B. Origin of carbon in fumarolic gas from island arcs. *Chem. Geol.* **1995**, *119*, 265–274. [CrossRef]

88. Marty, B.; Jambon, A. C/^{3}He in volatile fluxes from the solid Earth: Implication for carbon geodynamics. *Earth Planet. Sci. Lett.* **1987**, *83*, 6–26. [CrossRef]

89. O'Nions, R.K.; Oxburgh, E.R. Helium, volatile fluxes and the development of continental crust. *Earth Planet. Sci. Lett.* **1988**, *90*, 331–347. [CrossRef]

90. Tian, J.; Pang, Z.; Wang, Y.; Guo, Q. Fluid geochemistry of the Cuopu high temperature geothermal system in the eastern Himalayan syntaxis with implication on its genesis. *Appl. Geochem.* **2019**, *110*, 102–442. [CrossRef]

91. Claesson, L.; Skelton, A.; Graham, C.; Mörth, C.M. The timescale and mechanisms of fault sealing and water-rock interaction after an earthquake. *Geoflfluids* **2007**, *7*, 427–440. [CrossRef]

92. Zhou, X.C.; Wang, W.L.; Li, L.W.; Hou, J.M.; Xing, L.T.; Li, Z.P.; Shi, H.Y.; Yan, Y.C. Geochemical features of hot springgases in the Jinshajiang-Red River fault zone, Southeast Tibetan Plateau. *Acta Pet. Sin.* **2020**, *36*, 2197–2214. [CrossRef]

93. Sun, F.X.; Cui, Y.J.; Zheng, H.W.; Wang, Y.; Du, J.G. Hydrochemical response of hot springs around Hetao Basin to the 15 April 2015 M$_S$5.8 Alxazuoqi earthquake. *Earthquake* **2016**, *36*, 105–118. [CrossRef]

94. Li, J.; Li, Y.; Lu, L.N.; Sun, X.F.; Xie, C.; Cui, Y.J. Geochemistry of spring water in the Liupan Mountainarea. *Earthquake* **2017**, *37*, 61–72. [CrossRef]

95. Fulton, P.M.; Saffer, D.M. Potential role of mantle-derived Fluids in Weak Ening The San Andreas Fault. *J. Geophys. Res.* **2009**, *114*, B07408. [CrossRef]

96. Wiersberg, T.; Erzinger, J. Chemical and isotope compositions of drilling mudgas from the San and reas fault obser vatory at Depth (SAFOD) boreholes: Implications on gasmigration and theper-meability structure of the SanAndreas Fault. *Chem. Geol.* **2011**, *284*, 148–159. [CrossRef]

97. Hu, Y.T.; Zhang, Y.S.; Li, J.H. The relation between variations in concentration of trace elements and seismic activity. *Seismol. Gology* **1995**, *7*, 54–58.

98. Du, J.G.; Li, Y.; Cui, Y.J.; Sun, F.X. *Seismic Fluid Geochemistry*; Seismological Press: Beijing, China, 2018; pp. 1–2.

99. Kim, J.; Lee, J.; Petitta, M.; Kim, M.; Lee, K.K. Ground water system responses to the 2016 ML5.8 Gyeong earthquake, South, Korea. *J. Hydrol.* **2019**, *576*, 150–163. [CrossRef]

100. Wang, B.; Liu, Y.; Sun, X.; Ma, Y.; Zhang, L.; Ren, H.; Fang, Z. Hydrogeological and Geochemical Observations for Earthquake Prediction Research in China: A Brief Overview. *Pure Appl. Geophys.* **2018**, *175*, 2541–2555. [CrossRef]

101. Skelton, A.; Liljedahl-Claesson, L.; Wästeby, N.; Andrén, M.; Stockmann, G.; Sturkell, E.; Morth, C.M.; Stefansson, A.; Tollefsen, E.; Siegmund, H.; et al. Hydrochemical changes before and after earthquakes based on long term measurements of multiple parameters at 2 sites in northern Iceland-a review. *J. Geophys. Res. Solid Earth* **2019**, *124*, 2702–2720. [CrossRef]

102. Paudel, S.R.; Banjara, S.P.; Wagle, A.; Freund, F.T. Earthquake chemical precur sorsing round water:areview. *J. Seismol.* **2018**, *22*, 1293–1314. [CrossRef]

103. Chen, Z. *Hydrogeo Chemistry of the Hot Springs in Western Sichuan Province, South Western China after the Wenchuan MS8.0 Earthquake*; University of Science and Technology of China: Hefei, China, 2014. (In Chinese)
104. Liu, Y.W.; Cao, L.L.; Ping, J.J. Studing on typical characters offluid short termprecursory. *Earthq. Res.* **2004**, *20*, 372–379. [CrossRef]